



Report 2006

Second DELTA
User-Meeting

Dortmund
29th November 2006

Dear reader,

Like the first DELTA User Meeting held in 2005 the second will bring together as much DELTA users as possible. We would like to show the possibilities offered by a smaller synchrotron facilities and demonstrate its potential by the obtained results.

Promising work has been done in the present period of report (November 2005 – October 2006). The extended abstracts contained in this issue cover the wide range of activities at DELTA. You will find papers on infrared radiation, on VUV, on soft and hard X-rays applied to solve a variety of open questions in medicine, biology and material sciences. Some reports deal with fundamentals in physics and engineering.

I would also like to mention the successful presentation of DELTA at 9th International Conference on Synchrotron Radiation Instrumentation, Korea. We presented at international highest level an oral contribution and five posters. Without doubts this event was a highlight in 2006.

My last topic concerns the forthcoming DELTA User Meetings: It is easy to remember, the DELTA User Meeting will be held every year on the last Wednesday of November. You are cordially invited.

Dortmund, November 2006

Alex von Bohlen

Did you notice that DELTA's homepage is completely new? We are still missing some contributions. However, the first step is done and we are curios about the complete presentation of DELTA in the internet.

<http://www.delta.uni-dortmund.de>



Activities at Beamline 0

N. Nedelchev, E.H. Korte, ISAS – Institute for Analytical Sciences, Dortmund

Introduction

As shown in Fig.1 a cylindrical Cu mirror with vertical oriented axis accepting a horizontal fan of synchrotron radiation about 70 mrad wide is used to collimate and re-direct the infrared part through a beamline oriented radial to the electron orbit. The mirror accepts a similar vertical angle to cover the natural divergence up to wavelengths of almost $1700 \mu\text{m}$ (6 cm^{-1}). However, this acceptance angle is further obscured by the inner walls of the chamber. When infrared radiation shall be extracted the mirror is pushed in to a maximum of 29.5 mm (insertion depth) which strongly reduces the lifetime of the electron beam and injection is impossible. On a position of 26 mm the loss of the lifetime is acceptable and the mirror does not hamper injection. Depending on the insertion depth the mirror accepts radiation which originates from differently distant source points on the orbit and meets the mirror at different angles of incidence. Consequently the overall direction of the reflected beam varies and complete horizontal collimation cannot be achieved.

Angle adjustment

Due to a deviation of the light beam in horizontal direction, an angular adjustment of the mirror was necessary. A correction wedge was inserted between the mirror and the holder in order to cause a deviation of 2.4. Further and more precise, correction of the angular position of the output beam can be done after rigid fixing the table and defining a strategy for development of the beamline.

Calculations and experimental data comparison

The horizontal intensity profile of the reflected beam has been modelled by calculating a family of rays leaving the mirror at equidistant points. Neglecting the natural divergence of the radiation allows the waist of the fan to be used as common source of all rays considered. The development of the beam profile was studied up to a distance of about 5 m which would be enough to reach a spectrometer with a beamline straight through the wall. The results show that an effective collimation of the extracted radiation is indeed achieved. The calculations were performed for different distances of the mirror to the electron beam and insertion depths (Fig 2).

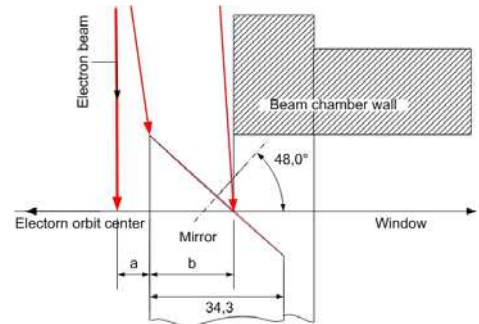


Fig 1. Scheme of the extracting mirror

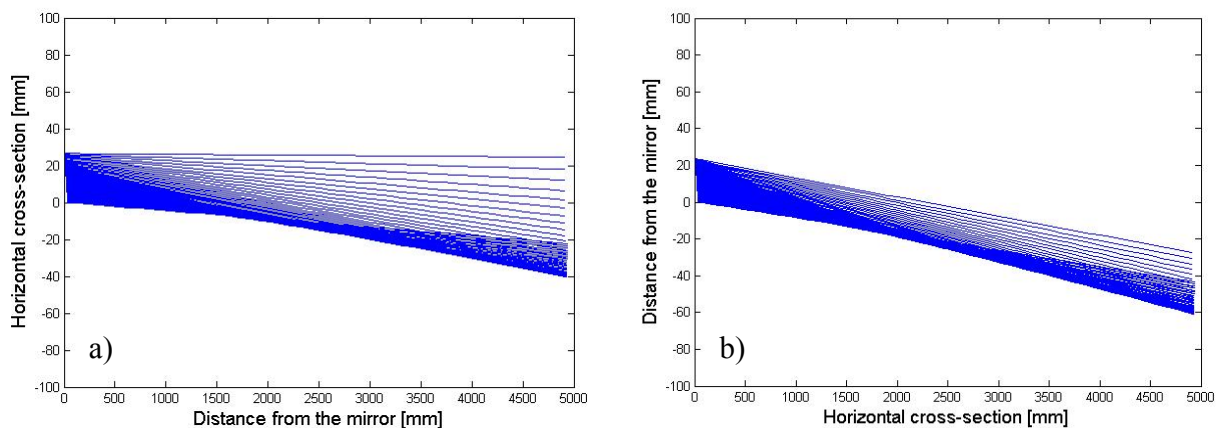


Fig 2. Theoretic horizontal ray tracing. Distance to the electron beam a: 6 mm – a); 9,5 mm – b) and insertion depth b: 29,5mm – a); 26 mm – b) (see Fig. 1)

Series of measurements have been made in order to determine the horizontal and vertical intensity distribution and compare it with the theoretical data. The output beam was scanned in steps of 1 mm, using 1 mm circular aperture on a detector system sensitive in the near infrared (max. sensitivity 1550 nm). A good agreement with the calculated horizontal distribution was observed. Furthermore a very good correlation of the natural opening angle with the experimental data for the measured wavelengths is found. The theoretic angle was calculated using the formula:

$$(1) \quad \Psi = 1,66(\lambda / \rho)^{1/3}$$

where λ is the wavelength and ρ is the radius of the electron beam orbit.

In the figure below, taken at 29.5 mm insertion distance, the observed second (sharper) maximum is most probably due to a reflection on the way between the extraction mirror and the quartz window. It is absent in scans with insertion distance 26 or 28 mm and ≥ 2.7 m away from the mirror.

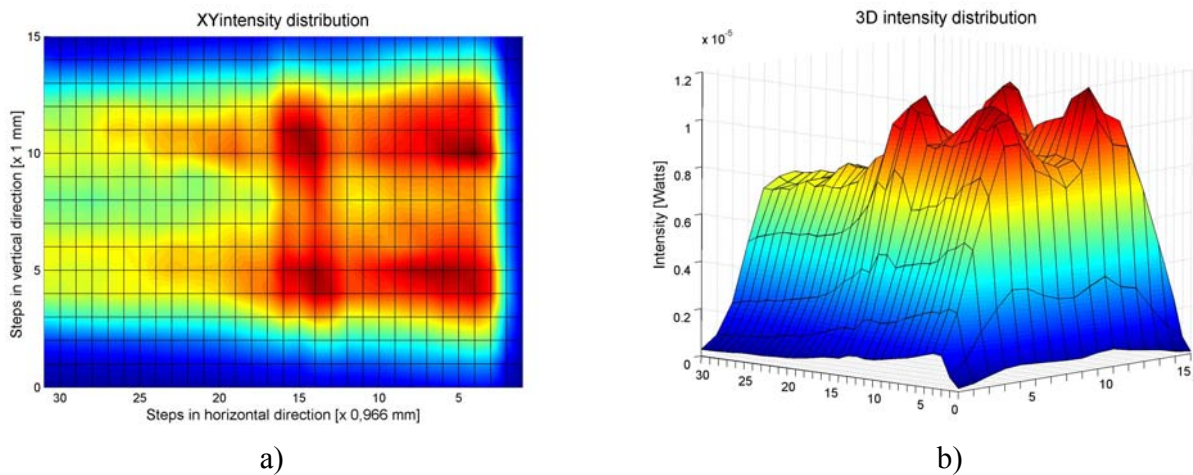


Fig. 3 Beam profile scanned directly after the quartz window:

a) top view, b) 3D-view. Current of the electron beam is ~ 90 mA (from 108 down to 80 mA) and the insertion distance is 29.5 mm, distance from the source point to the sensor ~ 1.1 m

Furthermore the beam profiles were scanned at several distances from the quartz window, starting from ~ 0.03 m up to ~ 4 m. Though the results agree with the theoretical predictions further measurements and the distribution of specific wavelength are required.

Status-Report BL2 - ISASLine

The ISAS Synchrotron Microprobe

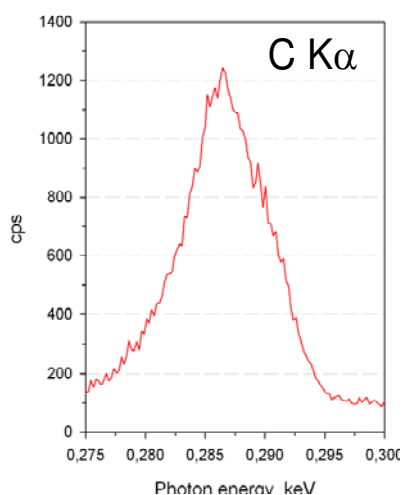
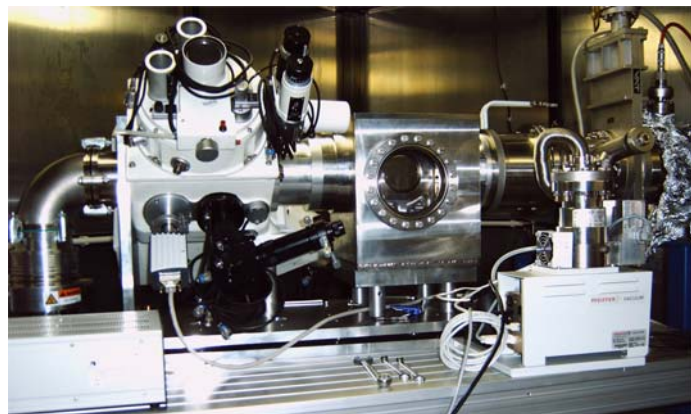
Alex von Bohlen, Markus Krämer, Roland Hergenröder
ISAS-Dortmund, <http://www.isas.de>

Since 2004 the ISAS operates the beamline BL2 at the synchrotron facility DELTA at University of Dortmund. An official contract between ISAS and DELTA has been signed before. Since this time synchrotron radiation (SR), an excellent excitation source for X-ray fluorescence spectrometry (XRF), is available at the “ISASLine”.

Among others, the high brilliance of the source in contrast to the conventional X-ray tube, the strong polarization of the radiation and the low divergence of the beam can be applied to XRF offering several advantages for spectroscopy. These outstanding features encouraged us to develop and operate a SR induced X-ray micro fluorescence probe connected to a wavelength dispersive spectrometer (SR-WDXRF). A relevant characteristic of such a device, namely, good lateral resolution at high spectral resolution can be applied for single spot-, line-scan and area map analyses of a variety of objects.

As reported last year, our prototype contains as an essential part the body of a scanning electron microprobe containing two focussing double crystal spectrometers. It was adapted and attached to the ISAS-Line.

The synchrotron radiation could be focused to produce a probe smaller than 15 μm in diameter. Even with this small probe the obtained counting rates for single fluorescence lines were of the order of some kcps.

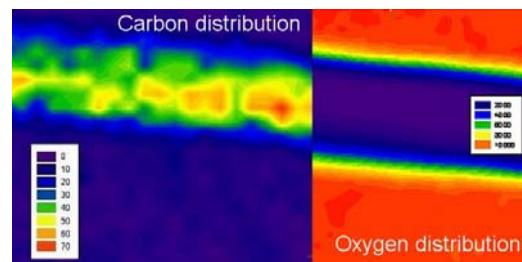


The SR-WDXRF micro fluorescence spectrometer operated under vacuum conditions was successfully used for the detection of light elements by their fluorescence K-lines (e.g. carbon, oxygen, nitrogen, fluorine, potassium, magnesium, aluminium, etc). Single spot analyses, line-scans and area maps were obtained in some minutes. Further elements are also accessible with high lateral resolution of some micrometers. They can also be detected with good spectral resolution strongly depending on used Bragg-crystal and on their respective K-, L- or M-lines. Typical HWFM values range between 3 eV and 30 eV.

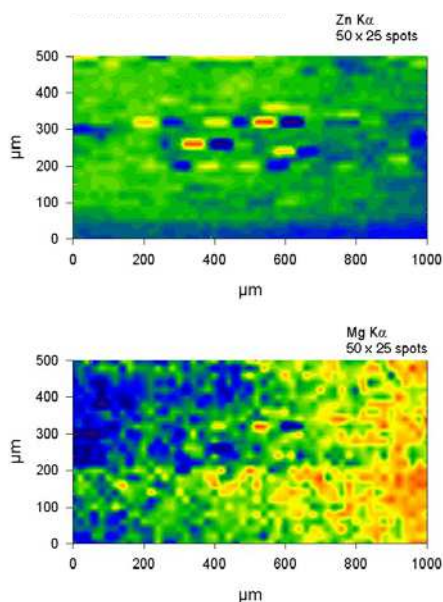
The method offers ideal conditions for the analysis of thin samples of non-conducting materials. This

potential could be applied to show the element distribution in plant material, in glass and in metal samples.

Exemplarily, the carbon distribution over a 300 μm branch of a fern (*Adiantum capillus-veneris*) mounted on a quartz glass is shown right. An apparent irregular distribution is due to geometric effects of the three dimensional shape of the branch. The oxygen distribution at the plane glass surface is homogeneous. A counting rate of 12000 ± 200 cps was observed at the free area (red).



Scan over a thin surface Mg/Zn passivation layer on steel.



The characterization of thin passivation Zn- and Mg-layers produced on steel for preventing corrosion was studied. Area-maps over larger areas (mm^2) can be obtained at moderate local distribution (probe size 15 μm diameter) in a short time. The non-homogeneous layers contained irregularities in the 50 *25 μm scale are due to small scratches in the direction of rolling of the steel during production. Additionally, both layers (Zink and Magnesium) are not of constant thickness as can be easily seen in the figure at left.

Outlook

The ISAS board of directors approved the extension of the ISASLine and decided the installation of a new double-crystal monochromator during the years 2006/7. The monochromator allows a more flexible and at the same time more specific excitation to X-ray fluorescence. The advantages clearly influence the quantification, it becomes easier, and in general, a more flexible and variable use of the beamline for additional applications is expected. Additionally, a precise goniometer will be installed at ISASLine for X-ray standing waves (XSW) measurements.

Report - U250 PGM
Beamline 5
“Spin Polarization at the Mg_xO_{1-x} / Fe and Mg_xO_{1-x} / Co interface:
the role of interfacial bonds”

Participants:

Frank Matthes, Martina Müller, Na Lei, Markus Gilbert, Stefan Cramm, and Claus M. Schneider

Institute of Solid State Research (IFF-9 “Electronic Properties”), Research Centre Jülich, 52425 Jülich, Germany

Contact: F.Matthes@fz-juelich.de

Motivation

The electronic band structure at the ferromagnet/isolator interface plays a decisive role for the functionality of tunneling magnetoresistive junctions, such as the single crystalline model systems Fe/MgO/Fe or Co/MgO/Co. This statement concerns not only the electronic properties of the individual components, like a high spin polarization of the ferromagnetic electrodes or the symmetry dependent attenuation of the electron wave functions in the gap of the isolator. Our work especially aims at the bonding conditions between ferromagnet and isolator that we can manipulate in a controlled manner.

In 2006, we have proceeded our work on the Fe/ Mg_xO_{1-x} interface and enlarge our activities to the Co/ Mg_xO_{1-x} system.

Experimental Setup

All experiments have been performed under ultrahigh vacuum conditions (base pressure $1 \cdot 10^{-10}$ mbar). The samples have been prepared on GaAs(100) substrates by electron assisted evaporation from material of high purity (99,995 % for Fe and Co rods, 99,98 % for Mg turnings). The crystal structure of bcc Fe and Co films were confirmed by low energy electron diffraction and possible oxygen and carbon contaminations were excluded using Auger electron spectroscopy. Subsequent, we have produced interfaces with an oxygen deficiency or excess using appropriate oxygen partial pressures during the growth of MgO. We performed core-level photoemission of the Mg 2p orbital to determine the Mg oxidation state in the Mg_xO_{1-x} films. Finally, the electronic band structures of such well characterized samples were investigated by spin- and angular resolved valence band photoemission spectroscopy.

Fe/MgO interface

a) stoichiometric MgO:

Upon coverage with MgO, we measure a stronger attenuation of the spectral weight for transitions originating from Δ_5 spin down initial states, when we compared them to those emerging from Δ_1 spin up states. The origin of this effect is not yet clear. Possible reasons could be a symmetry dependent change of the transition matrix elements upon MgO coverage (only within one-step photoemission model), a spin dependent scattering process at the Fe/MgO interface or a change in the electronic band structure that is caused by a relaxation of the vertical lattice constant for the outmost atomic Fe layers at the interface.

b) oxygen deficiency:

In this case, our photoemission experiments showed an increase of the spin polarization below E_F . We ascribe this change to a gain of transitions originating from Δ_1 spin up initial states. We explain our observation by hybridization with defects states in MgO. From scanning tunnelling spectroscopy experiments it was concluded that oxygen vacancies in ultrathin MgO films on Ag(001) will lead to localized defects states in the gap of the isolator, -1 eV below E_F [4]. These defect states have a symmetry similar to s-like orbitals and thus to our opinion may hybridize with the Fe Δ_1 spin up states. In contrast to Δ_5 , the symmetry of the Fe Δ_1 state contains contributions from wave functions pointing out of the surface/interface.

c) oxygen excess:

We measured a drop in spin polarization of the photoelectrons below E_F if we supply a surplus of oxygen during the MgO growth process. Additionally, we saw spectral changes of the Fe 3p core level that we interpreted as an indication for the formation of FeO, most likely at the interface. Theoretically assuming the existence of FeO at the interface, calculations by Zhang [5] have predicted a redistribution of charges from Fe Δ_1 states (directed perpendicular to the surface) to in-plane FeO bonds with Δ_5 symmetry character. This calculated redistribution would go conform to our measured decrease in spin polarization.

Co/MgO interface

a) pure bcc Co:

The spin polarized photoemission experiments showed four transitions in the spectra. Two transitions at higher binding energies: located at -1.4 and -1.9 eV below E_F with spin down and spin up character, respectively. These spectral features can be assigned to transitions emerging from Δ_5 and Δ_1 initial states of bulk bcc Co. Additionally, we observed two peaks located at -0,3 (spin down) and -0,5 eV (spin up) below E_F whose symmetry and origins are yet not undoubtedly clarified. A possible explanation is related to the tetragonal distortion of the bcc Co films[1] and would lead to a shift in energy of the Co bands. It is remarkable to notice, that transitions from the latter two initial states are not effected by coverage with any kind of above mentioned Mg_xO_{1-x} films.

b) stoichiometric MgO:

Similar to Fe, we see a clear suppression of the spectral weight that is related to transitions from Δ_5 spin down initial states. If we stay in the three step model of photoemission, our data lead to the conclusion that spin depending scattering at the Co/MgO interface can be excluded as an explanation for the observed drop in spectral weight from Δ_5 spin down initial states.

c) oxygen deficiency:

Spin polarized photoemission experiment from Co/MgO interfaces with oxygen vacancies displayed an increase of spectral weight that we believe to originate from Δ_1 spin up initial states. This behaviour is similar to the Fe/MgO interface, because states of the same symmetry are affected. But, the energetically coincidence of the localized defects states and the Δ_1 spin up states for Fe, is lifted in the case for Co. From the symmetry argument, we may conclude that the existence of neutral Mg (electronic configuration [Ne] $3s^2$) leads to an increased occupation of covalent bonds perpendicular to the interface.

Oxygen exposure to pure Fe and Co surfaces

Photoemission experiments of oxygen exposed to pure Co and Fe surfaces for a variety of coverages (up to several Langmuirs) have shown a stronger adsorption of oxygen at Fe surfaces, compared to that on Co. The presence of Mg at the surface, immediately leads to bonding with oxygen, even for small oxygen doses equal to a 1/20 part of a Langmuir.

Topic related publications

- [1] L.-N. Tong, C.-L. Deng, F. Matthes, M. Müller, C.M. Schneider, C.-G. Lee, "Influence of MgO overlayers on the electronic states of bcc Co(001) thin films grown on bcc Fe(001)/GaAs(001)", PRB 73(2006) 214401
- [2] M. Müller, F. Matthes, C.M. Schneider, "Photoemission study of the Fe(001)/MgO interface for varying oxidation conditions of magnesium oxide" (submitted)
- [3] M. Müller, F. Matthes, C.M. Schneider, "Spin polarization at ferromagnet-insulator interfaces: The beneficial role of stoichiometry in Fe/MgO" (submitted)

References

- [4] M. Sterrer, M. Heyde, M. Novicki, N. Nilius, T. Risse, H.P. Rust, G. Pacchioni, and H.J. Freund, J. Phys. Chem. B 110, 47 (2006)
- [5] X.-G. Zhang, W. H. Butler, and A. Bandyopadhyay, Phys. Rev. B 82, 092402 (2003)

Spin-resolved Photoemission Spectroscopy of amorphous CoFeB

M. Sperlich¹, R. Gadhimi¹, M. Matthes², T. Dimopolous³, J. Wecker³, C. Schneider² and G. Güntherodt¹

¹ II. Physikalisches Institut, Rheinisch-Westfälische Technische Hochschule Aachen

² Institut für Festkörperforschung, Forschungszentrum Jülich

³ Siemens Aktiengesellschaft, Corporate Technology, Materials and Microsystems

Tunnel magneto-resistive (TMR) junctions based on the system CoFeB/MgO/CoFeB show the highest TMR values of all FM/MgO/FM junctions (FM = ferromagnet) of up to 260% at room temperature ([1]-[6]). It could be shown that during annealing a crystallisation at the interface of the amorphous CoFeB/MgO occurs, which is supposed to increase the TMR to unprecedented values. The spinpolarisation of the ferromagnetic layers were estimated to about 75% [2].

By means of Spin-resolved Photoemission Spectroscopy (SP-PES) we investigated the spin polarisation of 23 nm thick amorphous Co₆₀Fe₂₀B₂₀ films. The samples were prepared ex situ at Siemens by DC magnetron sputtering and covered with a 2 nm ruthenium cap layer to prevent the oxidation of CoFeB. At DELTA the cap layer was removed in situ by Ar⁺-sputtering and the cleanliness was checked by Auger Electron Spectroscopy (AES). Despite the cap layer we could find a small contribution of oxygen in the AE-spectrum. Due to the rather high pressure of about 1×10^{-6} mbar during the sample deposition the oxygen is supposed to originate from the preparation.

After the surface treatment we investigated the spin-resolved photoemission spectra. We used the Jülich beamline at DELTA with the setup provided by the group of Prof. Schneider, Institut für Festkörperforschung, Forschungszentrum Jülich. The spin-resolved spectra were taken by a SPLEED-detector. The cleaned surface showed at a photon energy of $h\nu = 21.2$ eV a spin polarisation of about $(-14.9 \pm 3.4)\%$ at E_F (Fig. 1 (a)). According to a higher photoelectron scattering due to the amorphous state of CoFeB, we could find a higher contribution of secondary electrons in the spectra compared to epitaxial systems (not shown).

The influence of annealing on the spin polarisation was investigated by heating the sample to a temperature of about $T = 275$ °C for a total annealing time of 15, 30 and 60 minutes and by measuring after each annealing step. After the annealing the spin-resolved photoemission spectrum changed giving rise to the conclusion of a change in the electronic structure according to a crystallisation of the surface. The spin polarisation increased to a maximum of about $(-26.7 \pm 5.4)\%$ at an annealing time of 30 minutes (Fig. 1 (b)) and decreased to $(-17.6 \pm 2.0)\%$ upon further annealing for 60 minutes.

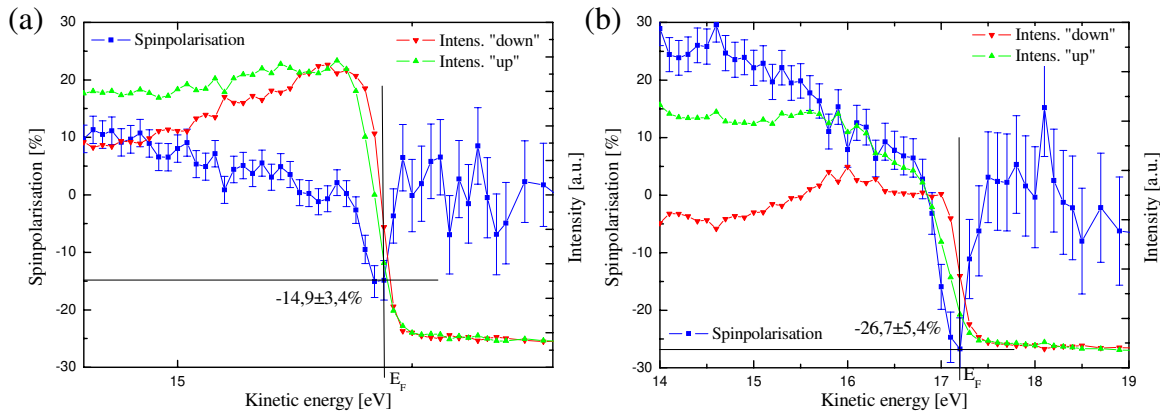


Fig. 1: Spin-resolved photoemission spectra of CoFeB after surface cleaning by Ar⁺-sputtering taken at $h\nu = 21.2$ eV. (a) Without any further treatment. The spin polarisation at E_F is $(-14.9 \pm 3.4)\%$. (b) After annealing at $T = 275$ °C for 30 minutes. The spin polarisation increased to a maximum of $(-26.6 \pm 5.4)\%$.

To investigate the influence of MgO on the spin polarisation at the CoFeB/MgO interface we deposited partly oxidised Mg on top of the CoFeB. At a coverage of approximately 1 Monolayer (ML) Mg we could not observe a significant difference in the spinpolarisation at E_F . We obtained a value of about $(-17.3 \pm 4.5\%)$ in comparison to $(-17.6 \pm 2.0\%)$ before. At a further coverage of about 1.5 ML, the spin polarisation at E_F decreased to $(-11.3 \pm 4.5\%)$ and at coverage of about 2.5 ML to $(-7.8 \pm 5.3\%)$. An annealing of 30 minutes at $T = 275 \text{ }^\circ\text{C}$ increased the spin polarisation to $(-15.2 \pm 4.2\%)$, which is nearly the same value as before.

In order to identify the different oxidation states of Mg we investigated the Mg-2p core levels [7]. The measurements were carried out at a photon energy of $h\nu = 88.3 \text{ eV}$. We could see a double-peak structure in the Mg-2p states at a 2.5 ML Mg coverage (Fig. 2 (a)). According to Thiry *et al.* [7] this could be explained by a mixture of metallic Mg and Mg with chemisorbed oxygen. After the annealing the spectra showed only one peak, which is shifted in comparison to the previous ones (Fig. 2 (b)). This could be explained by fully oxidised and ordered MgO. We conclude that the increase of the spin polarisation after the annealing from about -7.8% to -15.4% originates from the formation of a fully oxidised and well ordered MgO layer.

An exposure to oxygen at a pressure of 1×10^{-8} for 10 minutes and a further annealing for 15 minutes at $275 \text{ }^\circ\text{C}$ leads to a decrease of the spin polarisation to $(-1.3 \pm 3.6\%)$, which means that the spin polarisation practically vanishes. The additional amount of oxygen can form an oxidised layer of CoFeB at the CoFeB/MgO interface leading to a vanishing of the spin polarisation.

In conclusion, the oxidation of the sample seems to be as essential for a high spin polarisation as the crystallisation of the CoFeB/MgO. The difference in the calculated spin polarisation of 75% in comparison to the maximum measured spinpolarisation of about -26% at E_F originates from the different electronic states contributing to the tunnel effect on the one hand and the photoemission intensities on the other hand.

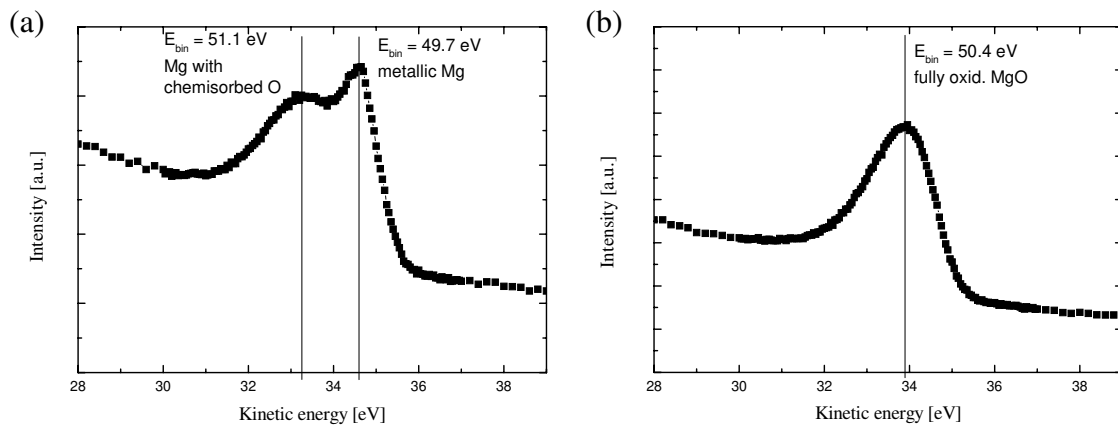


Fig. 2: Mg-2p-states measured at a photon energy of $h\nu = 88.3 \text{ eV}$. (a) After the deposition of about 2.5 ML partly oxidised Mg. According to Thiry *et al.* [7] the Mg exists in a metallic state and one with a contribution of chemisorbed oxygen. (b) After an annealing at $275 \text{ }^\circ\text{C}$ for 30 minutes only one shifted peak is left, indicating fully oxidised MgO.

- [1] Djayaprawira *et al.*, Appl. Phys. Lett. **86**, 092502 (2005).
- [2] Hayakawa *et al.*, Jpn. J. Appl. Phys. **44**, L587 (2005).
- [3] Cardoso *et al.*, J. Appl. Phys. **97**, 10C916 (2005).
- [4] Tsunekawa *et al.*, Appl. Phys. Lett. **87**, 072503 (2005).
- [5] Park *et al.*, J. Appl. Phys. **99**, 08A901 (2006).
- [6] Miao *et al.*, J. Appl. Phys. **99**, 08T305 (2006).
- [7] Thiry *et al.*, Phys. Rev. B **39**, 3620 (1989).

The Materials Science Beamline BL8 at DELTA

Abstract for the annual report 2006 of activities at DELTA

R. Wagner, D. Lützenkirchen-Hecht and R. Frahm

Fachbereich C-Physik, Bergische Universität Wuppertal, Gaußstraße 20, D-42097 Wuppertal

Several major steps have been accomplished in the commissioning of the beamline, e.g. the implementation of the experimental station for x-ray absorption fine structure measurements and determination of the energy resolution of the Si(111) monochromator crystals. Besides total photon flux measurements several EXAFS transmission measurements of Ni, Cu and Zn metal foils were made, and even the first QEXAFS data of the Cu K-edge were collected in 18 seconds with an energy resolution of 1 eV.

Implementation of the experimental XAFS station

The endstation for X-ray absorption fine structure measurements has been integrated into the existing diffractometer. The slit and detector systems have been constructed and implemented. The detector gas supply system has also been installed together with optional user gas connections.

Energy resolution of the Si(111) double crystal monochromator

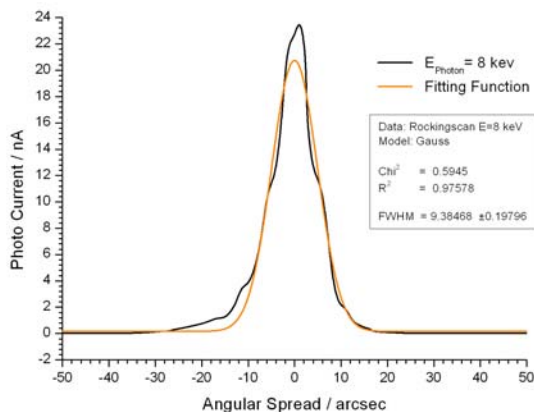


Figure 1: Rocking curve at 8 keV. Flux measurement with gas ionisation detector.

A portion of the white beam has been selected by the white beam slit system and traced through the non-dispersive fixed-exit Si(111)-crystal geometry into the experimental hutch. The photon flux was measured with a gas ionization chamber while rotating the second crystal in steps of sub arc seconds. The resulting rocking curve can be well approximated by fitting a Gaussian as depicted in figure 1. The angular spread is related to the resolution of the monochromator. At a photon energy of 8 keV the $\Delta\theta_{\text{FWHM}}$ amounts to 9.38 ± 0.19 arcsec compared to the theoretical figure of 7.83 arcsec. Another rocking scan, while detecting the beam intensity by means of a wire monitor, could reproduce those data. The broadening of the curves is due to the fact that an uncollimated beam was used and the crystal bender system to compensate for thermal deformation was not activated.

Photon flux measurement

The photon flux at the experiment as a significant property of the synchrotron radiation source has been determined from the photo current of a gas ionization detector behind a slit of 1 mm x 10 mm. The detector was filled with nitrogen, and the collecting electrodes were 130 mm long. The flux has been calculated taking into account the absorption of air between the exit window of the beam line and the detector entrance slit. A normalized photon flux of $6.7 \cdot 10^6$ photons/s/mA/mm² at 6 keV and $7.02 \cdot 10^6$ photons/s/mA/mm² at 9 keV has been determined, respectively. Those numbers are in good agreement with theoretical values for the superconducting asymmetric wiggler source.

EXAFS data

Data of a transmission absorption measurement of a 6 μm thin Ni foil are shown as an example. Other reference materials like Cu and Zn have been investigated in the same way. At the time the data were taken, the final data acquisition hardware and software had not been implemented, resulting mainly in a deterioration of the signal to noise ratio. Nevertheless, the data are already in good agreement with e.g. reference measurements carried out with another Si(111) monochromator, in this case the RÖMO II at the HASYLAB X1 beamline, as depicted in figures 2a-d. As can be seen from figure 2b the deviation of the two different data sets shown in 2a is always less than 2.5 %, while mostly under 1.5 %.

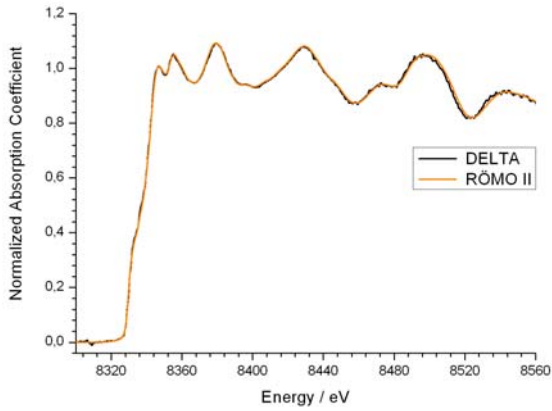
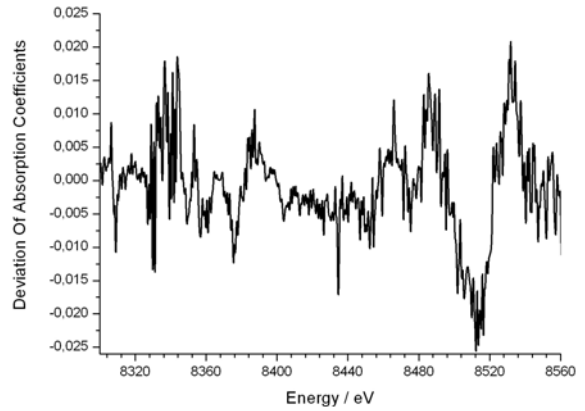
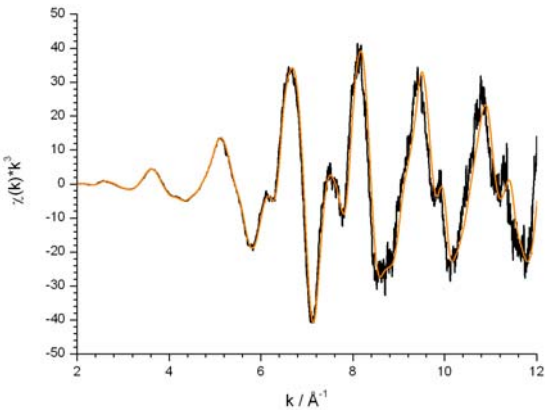


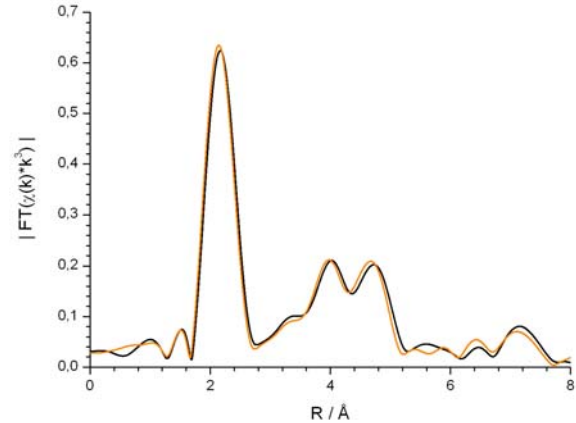
Figure 2: (a) Absorption at the Ni K-edge



(b) Deviation of the data sets



(c) EXAFS at the Ni K-edge



(d) Fourier transform of the EXAFS data

QEXAFS data

To further investigate the performance of the monochromator a quick absorption fine structure measurement at the end of the last beam time period, before the shut down in summer 2006, has successfully been accomplished. The scan was performed with an energy resolution of 1 eV within 18 seconds and the result of this QEXAFS scan at the Cu K-edge is shown in figure 3a. The conventional scan of the same sample in figure 3b is in very good agreement with the quick scanning procedure, which can be performed up to 30 times faster than the standard method.

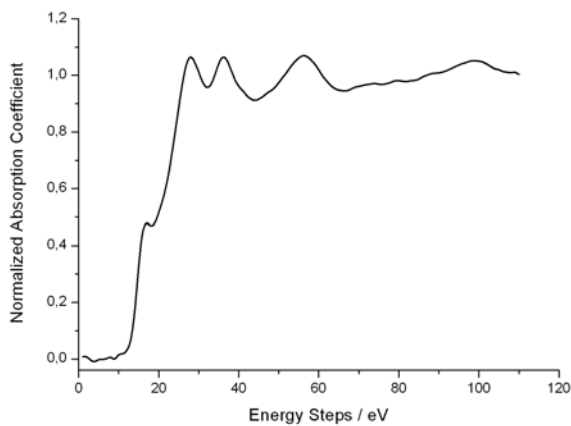
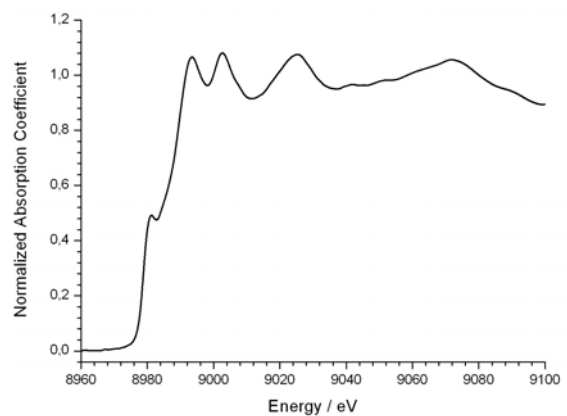


Figure 3: (a) Cu K-edge, QEXAFS data (18 s)



(b) Cu K-edge, conventional scan

Outlook

The optimization of the hard- and software for the data acquisition system is one of the next and most important goals during further commissioning. Furthermore, the calibration of the crystal bender system and the x-ray mirrors will be realized. To cover the whole energy range of the source the Si(311) and the YB₆₆(400) double crystal monochromators have to be commissioned, which includes the sagittal crystal bender for horizontal beam focussing using the second Si(311)-crystal.

Structural Properties of CoFeB/MgO Magnetic Tunnel Junction Multilayers

Miriana Vadalá, Arndt Remhof, Gregor Nowak, Kurt Westerholt and Hartmut Zabel

Institut für Experimentalphysik/Festkörperphysik,
Ruhr-Universität Bochum, D 44780 Bochum, Germany

Interfaces in magnetic tunnel junctions (MTJs) barriers and electrodes are of crucial importance to achieve high tunnelling magnetoresistance (TMR) values and thus in the overall performance of MTJ-based devices.

The interface roughness is known to affect the magnetic properties, especially the inter-layer coupling; moreover, interface stability with temperature is essential to preserve the characteristics of the stacking structure through the different stages of the processes required to build a device and in the expected working conditions.

In the last years efforts have been devoted to obtain aluminium oxide based tunnel barriers coupled with polycrystalline *3d* ferromagnetic metals and their alloys, with particular attention during the deposition process in order to minimize the formation of pinholes and impurities to increase the barrier quality [1].

A further improvement in minimizing the interface roughness occurred with the use of amorphous ferromagnets, mainly consisting of alloys of *3d* ferromagnets with metalloids such as Si or B, typically CoFeB, with reported values down to 0.4 nm in interface roughness [10].

The focus of the spintronics community is on Co₆₀Fe₂₀B₂₀/MgO based MTJs and TMR values above 200% at room temperature with a crystalline MgO tunnel barrier [2,3] have been already reported. At low temperature annealing, typically at 270°C, local CoFeB re-crystallisation occurs, whereas annealing up to 360°C leads to full recrystallization of CoFeB accompanied by an increase of the TMR values.

The annealing effects on the microstructure of these MTJs are presently not clear; we suppose that the restrictions in forming an ideally “smooth” CoFeB/MgO interface can be due either to the growing process or due to the intermixing, which gives rise to chemical roughness.

In the following we present structural results from the characterization of different series of CoFeB/MgO multilayers grown on a Si/SiO₂ substrate. Key parameters for the MTJs are the thickness of the respective layers, the growth and the annealing temperatures. They govern the degree of crystallization and the interface roughness. Small angle X-ray reflectivity measurements allow us to address especially thickness fluctuations and thereby to evaluate the interface roughness. Combined with off-specular scans, the correlation lengths can be determined [4].

The scans were performed at the BL9 [5] at a fixed X-ray energy of 11 keV.

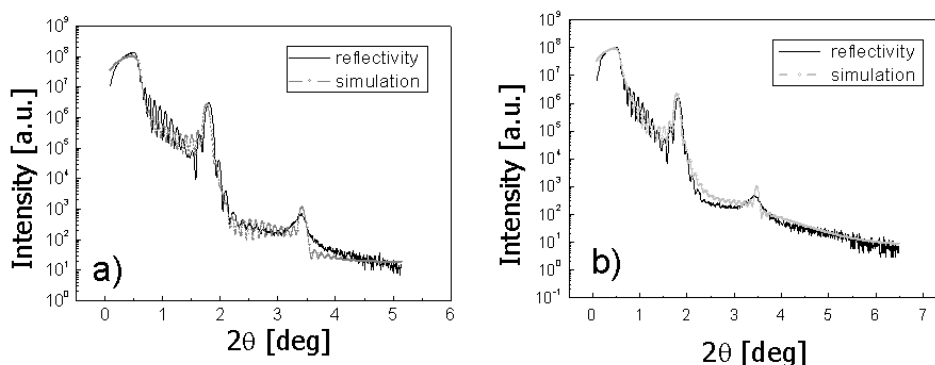


Figure 1) Reflectivity curves for two CoFeB/MgO thin films annealed at different temperatures: a) annealed at 360°C; b) annealed at 330°C.

Three sets of samples have been fully investigated: in the first series natural oxidation was employed to create the tunnel barrier, in the second series remote oxidation, and the third series was prepared by reactive plasma oxidation. Within each series different annealing temperatures were chosen to find out the optimum growth conditions and to check the thermal stability.

Fig. 1 displays two typical reflectivity curves for two $[\text{CoFeB}_{20} 30\text{\AA}/\text{Mg}+\text{Remot Oxid } 16\text{\AA}]\times 14$ samples belonging to the second series and annealed at different temperatures.

All measured reflectivity curves were modelled by a numerical fit (WinGiXA). Independently of the growth method and the treatment, all samples exhibit a rms roughness of about 5 Å. The kind of oxidation and obviously the annealing process do not influence this parameter.

Furthermore diffuse scattering scans in order to measure the in-plane correlations have been carried out. Fig.2 shows the rocking scans for four samples of the second series, recorded at the first Bragg peak, at different annealing temperatures. From the FWHM of the diffuse component we estimate a correlation length for the roughness of 10-15 Å.

All samples therefore show atomically flat and smooth interfaces. The interfaces are stable against heat treatment. However, their magnetic behaviour is different. In order to confirm these results, we performed PNR measurements which unveiled that this is due to the different densities of the oxide barrier, obtained by varying the stoichiometrics of the differently oxidized MgO layers.

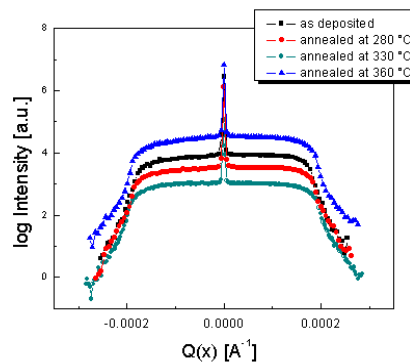


Fig. 2 Rocking scans taken in correspondence of the first Bragg peak, for four samples from the second series annealed up to 360°C.

To summarize, we found by XRR measurements that CoFeB/MgO ML can be grown with high structural quality and thermal stability. Their surface roughness is not the only parameter which governs the TMR of these systems, since all the samples show similar structural profiles but still quite different magnetic behavior.

We gratefully acknowledge the distinct support by Christian Sternemann and Michael Paulus during the experiment as well as the financial support provided through the European Community's Marie Curie actions (Research Training Networks) under contract MRTN-CT-2003-504462, ULTRASMOOTH."

[1] S. Cardoso, C. Cavaco, R. Ferreira, L. Pereira, M. Rickart, P.P. Freitas, N. Franco, J. Gouveia, N.P. Barradas, J. Appl. Phys. **97**, 10C916 (2005).
 [2] D.D. Djayaprawira, K. Tsunekawa, M. Nagai, H. Maehara, S. Yamagata, N. Watanabe, S. Yuasa, Y. Suzuki, K. Ando, Appl. Phys. Lett. **86**, 092502 (2005).
 [3] J. Hayakawa, S. Ikeda, F. Matsukura, H. Takahashi, H. Ohno, Jpn. J. Appl. Phys., Part 2 **44**, L587 (2005).
 [4] V. Holy, U. Pietsch, T. Baumbach, "High-Resolution X-Ray Scattering from Thin Films and Multilayers", Springer Tracts in Modern Physics 149, Springer, Berlin, Heidelberg, New York, 1999.
 [5] C. Krywka, M. Paulus, C. Sternemann, M. Volmer, A. Remhof, G. Nowak, A. Nefedov, B. Pöter, M. Spiegel, and M. Tolan, J. Synchrotron. Rad., **13**, 8 (2006).

Protein-Protein Interactions in Complex Cosolvent Solutions Revealed by Synchrotron Small-Angle X-ray Scattering in Combination with Liquid-State Theoretical Approaches

Nadeem Javid ^a, Karsten Vogtt ^a, Christof Krywka ^b, Metin Tolan ^b, and Roland Winter ^a

^a University of Dortmund, Department of Chemistry, Physical Chemistry I – Biophysical Chemistry, Otto-Hahn Str. 6, D-44227 Dortmund, Germany

^b University of Dortmund, Fachbereich Physik / DELTA, D-44221 Dortmund, Germany

Abstract

The effects of various kosmotropic and chaotropic cosolvents and salts on the intermolecular interaction potential of lysozyme (at pH 4.6, net charge +10) was evaluated at low to high protein concentrations by using synchrotron small-angle X-ray scattering in combination with liquid state theoretical approaches. The experimentally derived static structure factors $S(Q)$ obtained from the scattering intensity patterns of lysozyme solutions with and without added cosolvents and salts were analyzed with a statistical mechanical model based on the DLVO potential which accounts for repulsive and attractive interactions between the protein molecules. Different cosolvents and salts influence the interactions between protein molecules differently as a result of changes in the hydration level or solvation, of changes in charge screening, specific adsorption of the additives at the protein surface, or of increased hydrophobic interactions. Our scattering data indicate that intermolecular interaction effects are significant above protein concentrations of 1 wt%, and the scattering patterns for lysozyme concentrations above a few wt% exhibit strong intermolecular correlation peaks, already. With increasing protein concentration, the repulsive nature of $V(r)$ increases for pure lysozyme solutions. Kosmotropic cosolvents like glycerol and sucrose exhibit strong concentration dependent effects on the interaction potential, leading to an increase of repulsive forces between the protein molecules as a result of preferential hydration of the protein and hence

enhancement of the strength of its hydration layer. Trifluoroethanol (TFE) exhibits a more-phasic effect on $V(r)$ when changing the TFE concentration. For low alcohol concentrations, intermolecular interactions become more repulsive in nature, at higher TFE concentrations the attractive part of the interaction potential dominates, which might be due to a drastic decrease in dielectric permittivity of the medium and consequently increasing tendency of exposure of hydrophobic residues to solvent molecules, thus leading to partial unfolding and increased intermolecular hydrophobic interactions of the protein molecules. Salts like sodium chloride and potassium sulphate exhibit strong concentration dependent changes of the attractive interaction potential due to charge screening of the positively charged protein molecules. Guanidinium chloride at low concentrations exhibits a similar charge screening effect, resulting in increased attractive interactions between the protein molecules. At higher GdmCl concentrations, $V(r)$ becomes more repulsive in nature, however, which might - at least partially - be due to the presence of a high concentration of Gdm^+ ions binding to the protein molecules. We note that our findings also imply that in calculations of thermodynamic properties of proteins, in particular in cosolvent mixtures, activity coefficients may generally not be neglected in the concentration range above 1 wt% protein.

Structure analysis of CdSe nanoparticles

Lawrence Fon Teku and Ullrich Pietsch: Universität Siegen.

ABSTRACT

This project deals with the structure analysis of CdSe nanoparticles. For data analysis, a modified method is presented to provide precise structure information from nanoparticles in the range where common bulk-derived approaches fail. The method is based on the Debye equation which is incorporated in the refinement program call DISCUS, and allows us to determine the crystal structure and size of the particles with high precision. Detailed information on strain, relaxation effects, stacking faults, and shape of the particles become available. We find significant size differences between our results and those obtained by established methods from literature. This discrepancy is due to the presence of stacking faults in the nanocrystals that is caused by a mixed zinc-blende/wurtzite stacking and a significant lattice distortion which has not been considered by routine refinement approaches. Precise structure information is important for understanding the electronic and optical properties of both nanocrystals and their assemblies.

Modelling

The particles were simulated by creating an explicit list of all atomic coordinates using the program DISCU. The structure was assembled from Zincblende-like and wurtzite-like atomic layers. Initially the crystals were shaped in a columnar fashion of several stacks and subsequently all atoms outside a desired radius were removed in order to generate nanoparticles of approximately spherical shape. In order to study the local effects of strain, the lattice constants were adjusted. The powder diffraction intensities were calculated using the Debye formula..

The effective widths of the diffraction peaks are an intrinsic feature of the algorithm used and depend entirely on the size and defect concentration of the simulated nanoparticles. In contrast to the Rietveld refinement or Scherrer equation, no convolution is necessary to modify the peak widths; the resulting simulation is directly compared to the experimental diffraction pattern. Further, in contrast to the Scherrer equation approach, we calculate the intensity separately at each q value, i.e., we take into account that the structure factor changes within the broad q range of the diffraction maxima. This effect is neglected when the Scherrer equation is used, which convolutes the structure factor of a given Bragg reflection with a peak profile function to describe the broad diffraction peak. Moreover, the small size and high defect concentration within the nanoparticles renders the concept of Bragg reflections meaningless, since "Bragg planes" no longer exist.

Background subtraction is a crucial aspect of the data analysis. Despite the fact that parasitic scattering from amorphous materials and air was carefully avoided in the experiment, the tails of the direct beam remains a dominating part of the background. This is properly subtracted by fitting one Lorentzian profile fixed at $q=0$, i.e., at the position of the direct beam. Depending on the experimental conditions, an additional linear background is subtracted. The resulting background corrected powder pattern was simulated as described above. All essential structural features such as size, shape, atomic structure, atomic displacement parameters, stress and relaxation, stacking faults and vacancies are explicitly taken into account since they are intrinsic parameters of the nanoparticles model.

Data Analysis

The X-ray diffraction data was modelled by atomic clusters with about 100-500 atoms. The principal modelling procedure was carried out as follows: First we started with a manual refinement where spherical models with pure zinc-blende or pure wurtzite structure of different sizes were tested. Each time the lattice parameters were adjusted in order to obtain a good fit. We observed that the wurtzite structure fits some how better than the zinc-blende; hence we concentrated on the wurtzite structure in order to get an improve fitting. Next, the effect of stacking fault was tested on the wurtzite structure. With the introduction of a stacking fault, the fitting improved significantly. We also observe that non spherical models fitted the experimental data better. The effect of strain was studied by adjusting the lattice parameter. With manual refinement, we had enough clue to set starting parameters for the automatic refinement.

For the automatic refinement, we set an upper and lower limit for the lattice parameter. The stacking fault probability was set between zero and one. A stacking fault probability of one means the structure is pure zinc-blende while a stacking fault probability of zero means it is purely a wurtzite structure. The results of the automatic simulations for the nanoparticles studied are presented below together with corresponding parameters.

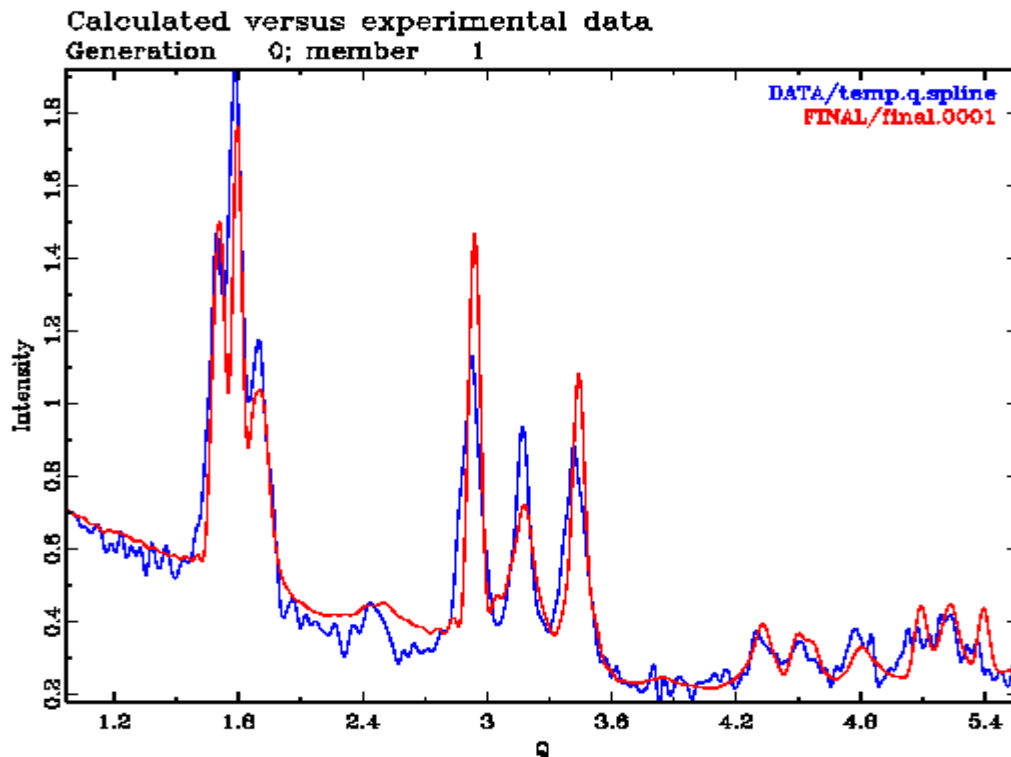


Fig.1 Calculated versus Experimental data. Blue is experimental data. While the red curve represent the calculated data.

Results obtained

- The nanoparticle have the wurzite hexagonal structure with a stacking fault probability of 0.22
- Lattice parameter: $a=b=4.31 \text{ \AA}$, $c=7.004 \text{ \AA}$ compared to $a=b=4.299 \text{ \AA}$ and $c.=7.010 \text{ \AA}$ respectively from literature
- The particles are non spherical with diameters of 4.56nm in the a-b plane and 4.8nm along c.

Synchrotron based X-ray diffraction study of Poly (3-hexylthiophene) – a π -conjugated polymer

- SIDDHARTH JOSHI¹, SOUREN GRIGORIAN¹, ULLRICH PIETSCH¹, ACHMAD ZEN²,
and DIETER NEHER² – ¹ Festkörperphysik, Universität Siegen, Siegen, Germany – ²
Institut für Physik, Universität Potsdam, Potsdam, Germany.

For few decades, there has been considerable interest in using organic semiconducting materials (polymers, oligomers) as the active component in organic field effect transistors (OFETs). This is mainly due to the fact that organic materials offer some advantages compared to the inorganic counterparts. Organic material is highly-soluble and can be easily processed using spin casting and printing technique, providing the possibility for the large-area electronic application. Also, it is mechanically tough and still flexible. Primarily, highly-soluble conjugated polymer is among the most promising material for OFET devices. Poly (3-hexylthiophene) P3HT is one of the most promising π -conjugated polymers used in polymer-electronics and exhibits relatively high charge carrier mobility. However, up-to now the correlation between the surface morphology and the charge-carrier mobility in P3HT is still not well-understood. Our studies are focussed on the investigation of the structural order [1] and the degree of crystallinity of semi-crystalline thin films (thickness \sim 10-50 nm) of low-and high-molecular weights of P3HTs by using X-ray scattering techniques. Further, there are some fundamental problems which we want to solve by using synchrotron radiations, namely: 1) How does the degree of crystallinity influence the mobility in different weight fractions of P3HT; 2) How the film structure varies with temperature; and (3) How the structure of the P3HT films correlates to the morphology at the SiO₂/P3HT interface.

For detailed studies, grazing incidence X-ray diffraction (GID) [2, 3,] (fig. 1 right) has been employed in order to determine the vertical and lateral structures of P3HT films. Additionally, X-ray reflectivity technique has been used to obtain the average thickness of the thin films (fig. 1 left). All the measurements shown in here have been measured at the BL 9 beam-line of DELTA synchrotron source, Dortmund, Germany. Based on the additional investigations using atomic force microscopy (AFM), transmission electron microscopy (TEM) and X-ray measurements, we concluded that the thin film of low molecular weight fraction samples consist of highly ordered crystallites with ribbon- or whiskers- like structures embedded in an amorphous matrix. Further, the smaller charge-carrier mobility in low-M_w films is mainly due to the charge-carriers are scattered around the amorphous region. In contrast, the higher mobility in high-M_w fraction can be explained by the fact that high M_w fraction consists of small partially-ordered domains, with average width smaller than the chain length. Thus, chains either fold back, extend into the disordered phase, or interconnect neighboring domains, which led to an efficient interchain transport. Also, we have determined the degree of crystallinity for low-and-high molecular weight fractions utilising Ruland's method [4] indicating the increase of degree of crystallinity with increasing the concentration of the samples. From temperature dependent reflectivity measurements in low-M_w fraction, we have found that there is an increase in thickness of ca. 30%, if we compared the measurement at room temperature with the one at the melting transition of the material. Out-of-plane measurements indicate that the structure order peaks intensity is decreasing at elevated

temperatures (fig. 1 right) and it disappears completely at the melting point, which suggests that the polymer is now completely amorphous. The inter-planer distances ‘d’ increases at the higher temperature (fig. 2 left). Interestingly, the intensity of thinnest film of concentration (1mg/mL, thickness 11 nm) shows that the crystal structure remains constant up to ~ 70 °C and afterwards decreases sharply (fig. 2 right), which is in contrast to the observed trend in the thicker samples. However the second curve of (1mg/mL, thickness 17 nm) does not shows the same trend due to the different preparation conditions. This can be explained by the fact that there is a strong substrate-layer interaction.

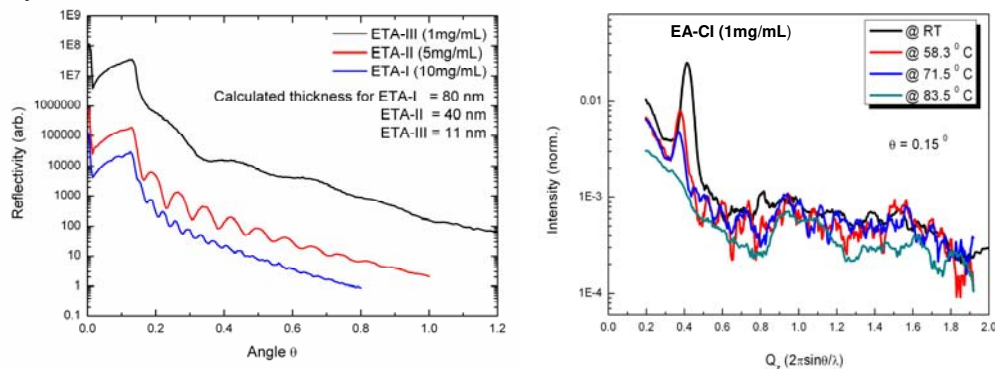


Fig. 1. X-ray reflectivity & Out-of-plane temperature dependent scan for ethyl acetate fractions (ETA) (1mg/mL) for $\theta = 0.15$ ° at beam line BL9, Delta.

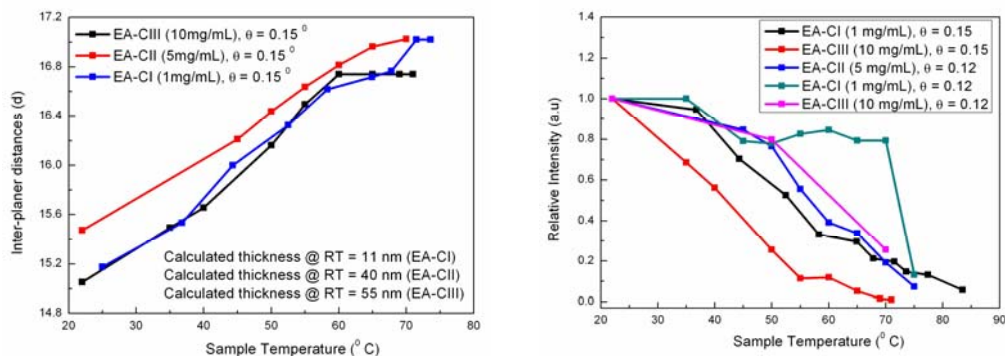


Fig. 2. ‘d’ spacing and the relative intensity versus temperature for different ETA’s fractions of P3HT.

1. A. Zen et al., *Macromolecules*, 39 (2006) 2162.
2. R. J. Kline et. al., *Nature materials*, 5 (2006) 222.
3. A. Zen et al., *Adv. Funct. Mater.* 14 (2004) 757.
4. W. Ruland, *Acta Cryst.*, 14 (1961) 1180.

Acknowledgement: We would like to thanks all the BL9 beamline staff members at Delta synchrotron source, Dortmund, Germany for their help during the measurement. At the same time we also thanks to Prof. Ullrich Scherf (University of Wuppertal) and Dr. Silvia Janietz (IAP, Golm) for providing fractionated polymer samples. This work was financially supported by the DFG under the project of emphasis: SPP 1121.

Study of the disproportionation in bulk amorphous germanium monoxide

Andreas Schacht¹, Christian Sternemann¹, Achim Hohl², Henning Sternemann¹, Michael Paulus¹, and Metin Tolan¹

¹ *Experimentelle Physik I/DELTA, Universität Dortmund, Otto-Hahn-Str. 4, D-44221 Dortmund,*

² *Institut für Materialwissenschaften, TU Darmstadt, Petersenstr. 23, D-64287 Darmstadt*

(Dated: October 30, 2006)

Measurements of the x-ray absorption near-edge structure at the Ge K-edge of ex-situ annealed amorphous germanium monoxide, i.e. GeO_x ($x \approx 1$), samples were accomplished in partial fluorescence yield mode at BL9 of the synchrotron radiation source DELTA utilising a spectrometer in Rowland geometry. A systematic temperature dependence was observed for the near-edge structure within the first 10 eV above the Ge K-edge and could be related to the disproportionation of amorphous germanium monoxide into germanium and germanium dioxide. The onset of the observed disproportionation process was estimated to a temperature of about 245°C. For samples annealed above 500°C crystallisation was found which could be confirmed by x-ray diffraction.

Bulk amorphous germanium monoxide (a-GeO) is – analogous to amorphous silicon monoxide (a-SiO) – of valuable interest for optoelectronics (e.g. coatings, devices) [1–3]. So far no structure model is established for a-GeO but it is assumed that it is not disproportionated into pure Ge and GeO_2 in its native state comparable to the case of a-SiO [4, 5]. Aim of this work is the study of disproportionation in a-GeO induced by temperature treatment of a-GeO samples via the measurement of the x-ray absorption near-edge structure (XANES) at the Ge K-edge.

The native a-GeO samples were synthesised at the TU Darmstadt by A. Hohl in an induction vacuum sintering system in a comparable way to the usual production of a-SiO. The films were prepared by evaporation of a Ge/ GeO_2 powder mixture in vacuum at 1000°C and subsequent condensation at a deposition rate of about 10 Å/s on a molybdenum (Mo) substrate at approximately 100°C. So a several μm thick a-GeO layer on Mo substrate was obtained. Afterwards the substrate with the a-GeO film was cut into $10 \times 10 \text{ mm}^2$ pieces. Before the experiment five samples were annealed for 30 minutes in an oven at 200, 300, 350, 375, and 400°C, respectively (The samples are denoted as GE, GG, GW, GR, GV.). Moreover, one native sample (GC) was annealed ex-situ during the experiment in the range of 275°C up to 425°C and in addition three other samples were annealed at temperatures of 525 (GR), 625 (GS) and 725°C (GU). These samples were placed into an evacuated ($\sim 10^{-6}$ mbar) quartz-glass tube and were heated for about 30 min. The unannealed sample GT serves as a reference.

All measurements were performed at BL9 of the 1.5 GeV synchrotron radiation source DELTA [6]. Due to the fact that the a-GeO samples have to be synthesised as a film on a substrate transmission mode measurements of the XANES were not possible. Therefore, measurements of partial and total fluorescence yield have been accomplished using the modified Rowland spectrometer and a NaI scintillation detector, respectively. The analyzer energy of the Rowland spectrometer was set to the maximum of the Ge K_{α_1} fluorescence line at 9886.4 eV at an excitation energy of 11200 eV. Then the incident energy was scanned in the range of 11095 eV up to 11050

eV to measure the absorption edge in partial fluorescence yield detection. Several single spectra were accumulated, checked for consistency, and added up finally.

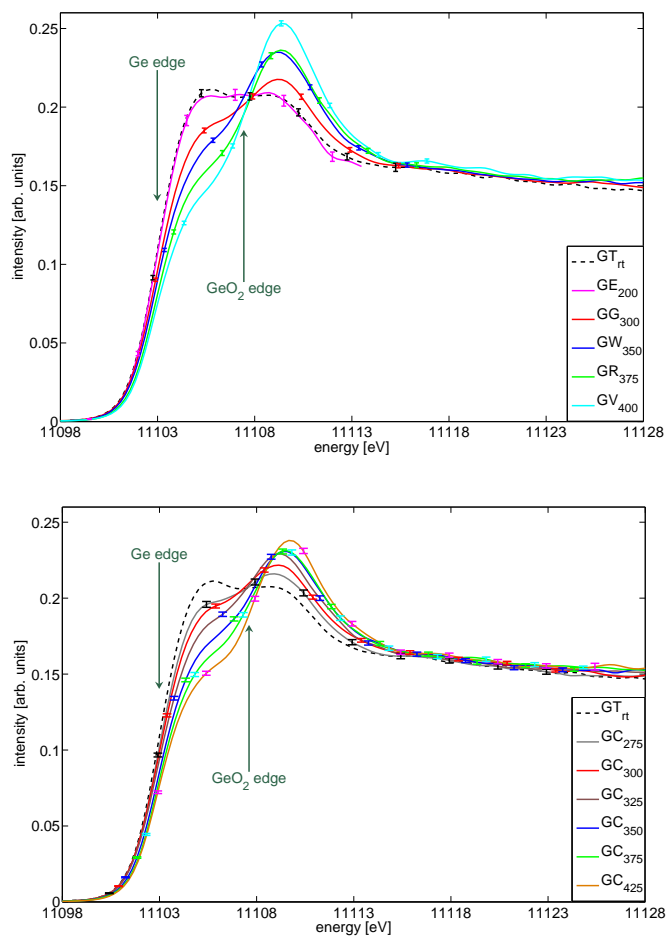


Figure 1: *Normalised XANES spectra of five different a-GeO samples annealed in the range of 200°C to 400°C (top) and of the GC sample heated from 275°C up to 425°C (bottom). The native sample (GT) serves as a reference in both figures. The arrows indicate the energy positions of the Ge and GeO_2 K-edge.*

The summed spectra were normalised to the incident intensity and shifted in energy to match the onset of the

Ge K-edge at 11103 eV. Finally, all spectra were normalised to the integral intensity in the energy range between 11098 eV and 11145 eV.

The measured XANES spectra of the differently annealed a-GeO samples are presented in Fig. 1. The spectrum of the native sample shows a distinct two peak structure. The shape of this spectrum cannot be modelled by a simple stoichiometric superposition of a Ge and a GeO₂ absorption spectrum. Therefore, the shape gives a strong indication that a-GeO is not disproportionated into Ge and GeO₂ in its native state, although a direct observation of suboxidic contributions (i.e. Ge(Ge_{4-x}O_x) with $x = 1, 2, 3$) is not possible in the shape of the edge onset due to the limited experimental resolution.

With increasing temperature a shift in spectral weight of the two structures related to the Ge and GeO₂ edge onset is observed and the spectra become similar to a superposition of pure Ge and GeO₂ spectra. This systematic behaviour is shown in Fig. 1 for two different sample series.

A more detailed analysis of the disproportionation process is done by subtracting the reference XANES spectrum of the native sample GT from each annealed spectrum. Then the obtained difference is integrated between 11098 eV to 11108 eV to characterise the contributions to the total spectrum related to Ge and the corresponding suboxides Ge(Ge_{4-x}O_x) with $x = 1, 2, 3$. The integral values ΔS are presented in Fig. 2 for the two different series. Moreover an averaged value is shown if values of the two series for the same temperature are available. A strong reduction of ΔS , and thus a reduction of suboxidic contributions, can be observed for temperatures above 250°C. By a linear fit of ΔS values for temperature above 275°C the onset of disproportionation can be

determined to $T_{\text{onset}} = 245 \pm 20^\circ\text{C}$ as indicated in Fig. 2. A more detailed analysis of the spectra is in progress along with a preceding characterisation of the measured samples with complementary experimental methods.

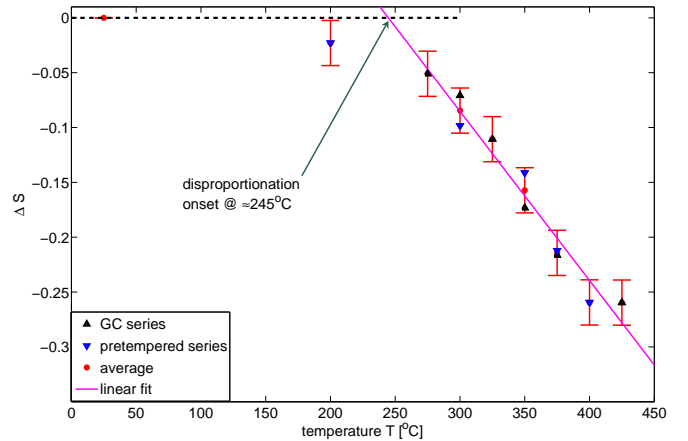


Figure 2: Decreasing contribution ΔS of Ge suboxides to the absorption edge onset as a function of temperature T (see text for details).

Beyond the study of XANES in fluorescence yield mode x-ray diffraction measurements of all samples were accomplished. Up to 500°C no crystallisation of the samples could be observed. Tempering of the amorphous samples at temperatures above 500°C results in partial crystallisation of the Ge and GeO₂ constituents after disproportionation.

We would like to thank the DELTA machine group for providing synchrotron radiation and technical support.

-
- [1] T. Ohta, M. Takenaga, N. Akahira, T. Yamashita. *J. Appl. Phys.*, **53**, 8497 (1982).
 [2] F. Vega, C. N. Afonso, J. Solis. *Appl. Surf. Science*, **69**, 403-406 (1993).
 [3] K. Prabhakaran, T. Nishioka, K. Sumitomo, Y. Kobayashi, T. Ogino. *Appl. Phys. L.*, **62**, 864-866 (1993).
 [4] A. Hohl, T. Wieder, P.A. van Aken, T.E. Weirich, G. Denninger, M. Vidal, S. Oswald, C. Deneke, J. Mayer,

- H. Fuess. *J. Non-Cryst. Solids*, **320**, 255-280 (2003).
 [5] C. Sternemann, J.A. Soininen, M. Volmer, A. Hohl, G. Vanko, S. Streit, M. Tolan. *J. Phys. Chem. Solids*, **66**, 2277-2280 (2005).
 [6] C. Krywka, M. Paulus, C. Sternemann, M. Volmer, A. Remhof, G. Nowak, A. Nefedov, B. Pter, M. Spiegel, M. Tolan. *J. Synchrotron Rad.*, **13**, 8-13 (2006).

Study of the carbon dioxide adsorption on silicon via high energy reflectivity

Daniela Lietz, Michael Paulus, Christian Sternemann, Metin Tolan

Exp. Physics E1a/DELTA, University Dortmund, Otto-Hahn-Str.4, 44221 Dortmund, Germany

1 Introduction

An experiment at the beamline 9 of DELTA has been prepared in order to investigate the adsorption of carbon dioxide (CO_2) on a silicon wafer. Therefore, the layer thickness and roughness are determined in dependence of the CO_2 -pressure via X-ray reflectivity. This method is well suited to determine the electron density profile, the layer thickness (d_{layer}) and the roughness (σ). Because the condensation pressure of CO_2 at 0°C is 34 bar (figure 1) a high pressure cell has been constructed which has two aluminum windows of 1 mm thickness. To penetrate this aluminum windows with the x-ray beam high photon energy is needed. Due to this fact the experiment has been accomplished at the DELTA beamline 9 at 27 keV (wavelength $\lambda = 0.459\text{\AA}$).

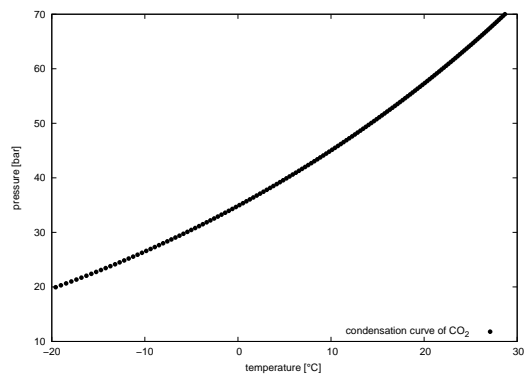


Fig. 1: Condensation curve of CO_2
(<http://webbook.nist.gov/chemistry>)

2 Experimental Setup

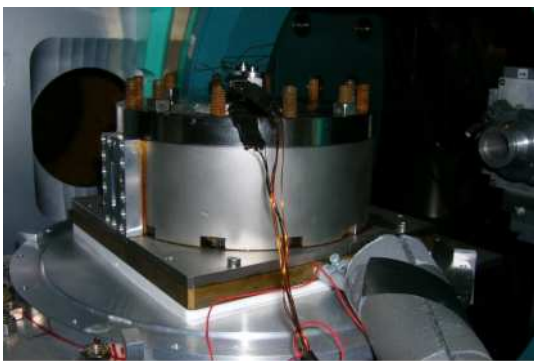


Fig. 2: The high pressure cell

was fixed in the middle of the pressure cell. The samples temperature ($T = 1^\circ\text{C}$) was controlled by a Lakeshore temperature controller with an accuracy of $\pm 0.05^\circ\text{C}$. At $T = 1^\circ\text{C}$ a pressure of 35 bar was needed to condense the CO_2 . In order to observe different degrees of adsorption the gas pressure was increased in 17 steps from 0 bar (pure wafer under Helium atmosphere) to 34.4 bar. For each pressure step an x-ray reflectivity was

A picture of the sample cell is shown in figure 2. The beam enters the cell at the right side, hits the sample under an angle of θ , is reflected by the samples surface and leaves the sample cell on the left side. The reflected beam is detected under an angle of 2θ using a NaI(Th) point detector. The typical incidence photon flux at 27 keV photon energy was about $6.5 \cdot 10^8 \frac{\gamma's}{\text{mm}^2}$ at 100 mA beam current. The used sample cell is made of stainless steel and has a wall thickness of 1 cm. The windows are made of 1 mm thick aluminum (fig. 2). The silicon wafer

recorded. For determination of the diffuse scattered radiation every reflectivity was followed by a longitudinal diffuse scan with a detector offset of 0.1° to the specular condition. The measuring time for each pressure step was about 1.5 hours.

3 Results

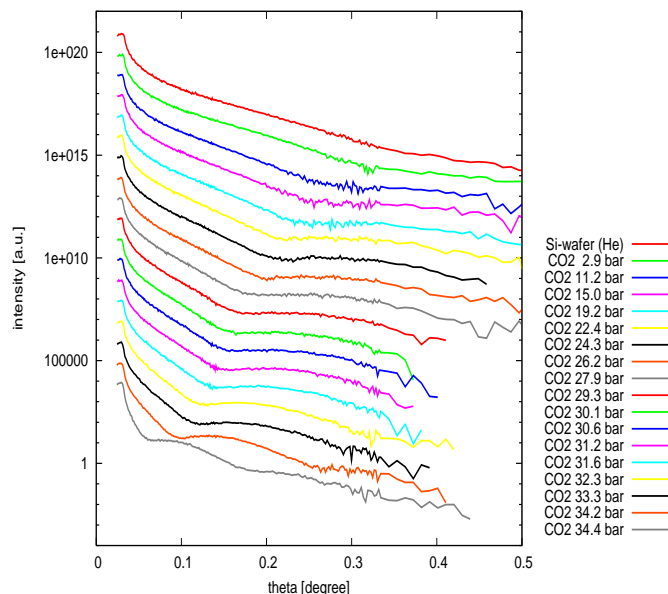


Fig. 3: Measured reflectivity curves of CO_2 at different pressures

In figure 3 some x-ray reflectivities are shown. In reflectivity experiments the incident wave is reflected at the substrates and the layers surface leading to characteristic oscillations, Kissig fringes, in the reflectivity.

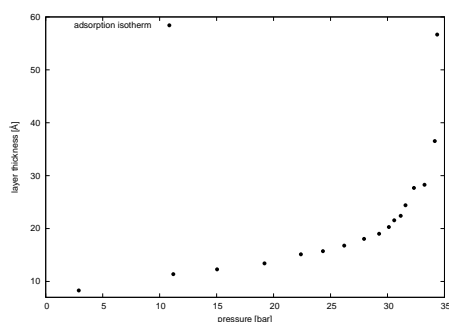


Fig. 4: Adsorption curve of CO_2

The width between the oscillation maxima or minima corresponds to the difference of the momentum transfer perpendicular to the surface (Δq_z) which is connected with the layers thickness d_{layer} via $d_{\text{layer}} = \frac{2\pi}{\Delta q_z}$. In figure 3 one can clearly see the development of the expected oscillations with increasing pressure.

The measured reflectivities are refined with the use of the effective density model. The layers thickness, roughness and dispersion were determined as well as the substrates structure. The adsorption isotherm (d_{layer} vs. pressure) is shown

in figure 4. As anticipated the thickness of the gas layer increases with rising pressure. The layers roughness shows an increase with the layers thickness which is due to the interaction between the substrate and layer surface which smoothes the layers surface especially at low layer thickness.

From the adsorption isotherm one can calculate the Hamaker constant in order to draw conclusions about the interaction between substrate and layer and to calculate the layers roughness. This data analysis is still in progress.

We would like to thank the DELTA machine group for providing synchrotron radiation and technical support.

MPIE User Report

1. Project

Phase characterisation of thin oxide scales grown on FeAl alloys

T. Liapina*, D. Vogel*, Ch. Sternemann and M.Spiegel*

* MPI für Eisenforschung GmbH

2. Introduction

Previous investigations on the initial stages of oxidation of iron aluminides at temperatures below 1000 °C revealed a formation of double oxide layer consisting of an outer iron-rich oxide followed by an inner α -Al₂O₃ layer. However, metastable alumina formation is assumed to take place during the initial stages of oxidation, preferably at lower temperatures. The formation of stable corundum may be explained by two reasons:

1. Metastable phases are formed even earlier in the oxidation process and the phase transformation to α -Al₂O₃ is finished after annealing time used in [1] (5h);
2. Fe₂O₃ favours the nucleation of α -Al₂O₃ due the strong similarities in the crystallographic oxide structures.

The aim of the present study is to identify alumina phases formed after short oxidation times as well as to clarify the role of hematite in the formation of stable α -Al₂O₃. To this end first, oxidation has been carried out in air as well as in an atmosphere with low oxygen pressure in order to prevent hematite formation. Moreover, the oxidation of ternary iron aluminides was investigated in order to prove protective alumina formation and to identify possible oxides of third elements.

3. Experimental

Cast polycrystalline binary and ternary alloys of composition Fe-15 at.% Al and Fe-26 at.% Al with alloying elements Ta, Ti and Nb (4 at.%) were produced by inductive melting. Oxidation of was carried out for 5 min at 700°C to 900°C for the binary systems and of Fe-26 at.% Al-4 at.% X (with X = 0, Ta Ti and Nb) for 5 h at 700°C both in synthetic air and N₂-5 vol.% H₂ (dew point -40°C) gas mixture.

As reference samples for adjusting the measurement set-up at the DELTA diffractometer beamline model oxides of 250-300 nm thickness consisting of Fe₂O₃ (hematite) on a Pt substrate were produced. For all grazing incidence X-ray diffraction (XRD) measurements the incidence angle was 0.3° and a primary beam energy of 13 keV was used.

4. Results

1. Fe-15 at.% Al oxidised at 700°C to 900°C:

a) in synthetic air.

Fe-15at.%Al samples oxidised at 700°C, 800°C and 900°C for 5 minutes yield a two layered oxide scale of Fe₂O₃ (hematite) and Al₂O₃ (corundum) composition. Figures 1 to 3 show the corresponding grazing incidence diffraction patterns where three phases are well detectible – hematite, corundum and α -iron. α -iron is visible due to the penetration depth (estimated 600 nm) is larger than the double oxide layer thickness (ranging from 80 nm at 700°C to 180 nm at 900°C according to XPS measurements).

This findings agree well with earlier results [Delta report 2005] where the oxidation was carried out for 5 hours. They show very clear that even in the initial stages of oxidation the formation of stable α - Al_2O_3 takes place. Corundum reflections become more pronounced at higher oxidation temperature. The oxide layer thickness also increases with the temperature that leads to weakening of matrix reflections. No Al_2O_3 polymorphs like γ - or θ - Al_2O_3 were detected.

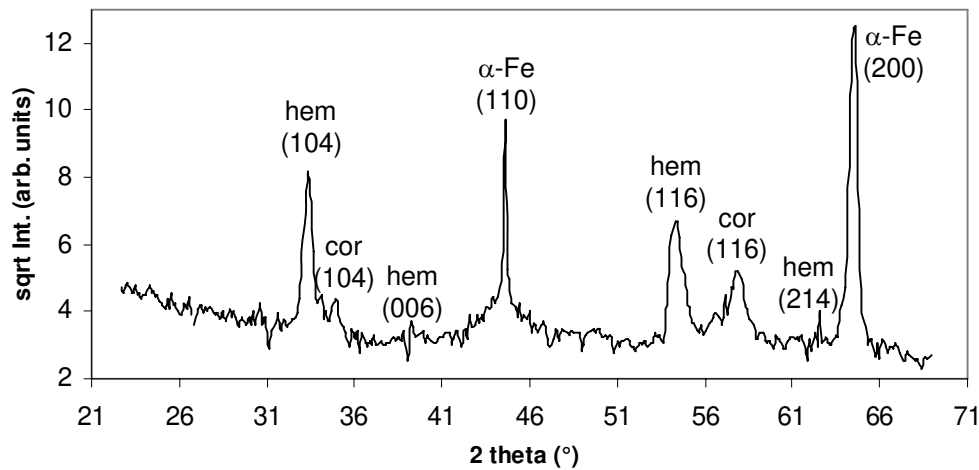


Fig.1: Fe-15at.%Al oxidised at 700°C / 5min / syn.air; incidence angle (θ) = 0.3° (interaction depth ~ 600 nm); phases identified: hematite, corundum and α -Fe structure.

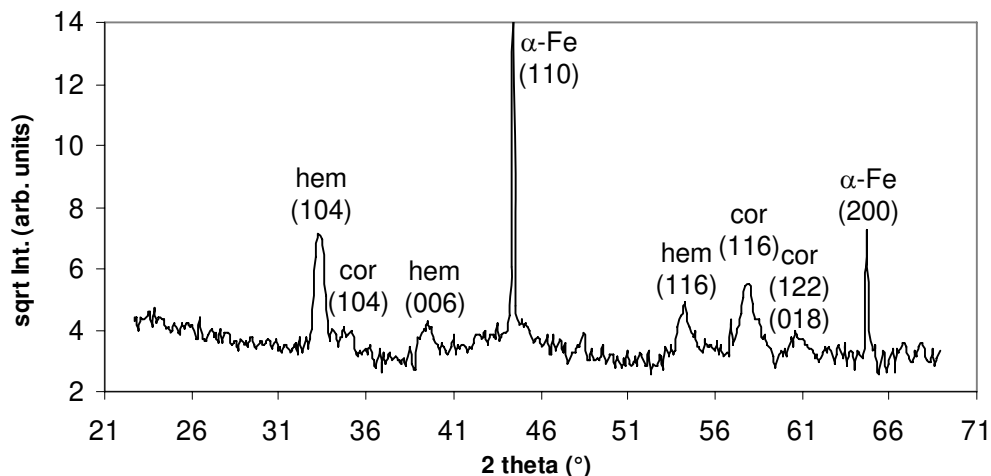


Fig.2: Fe-15at.%Al oxidised at 800°C / 5min / syn.air; incidence angle (θ) = 0.3° (interaction depth ~ 600 nm); phases identified: hematite, corundum and α -Fe structure.

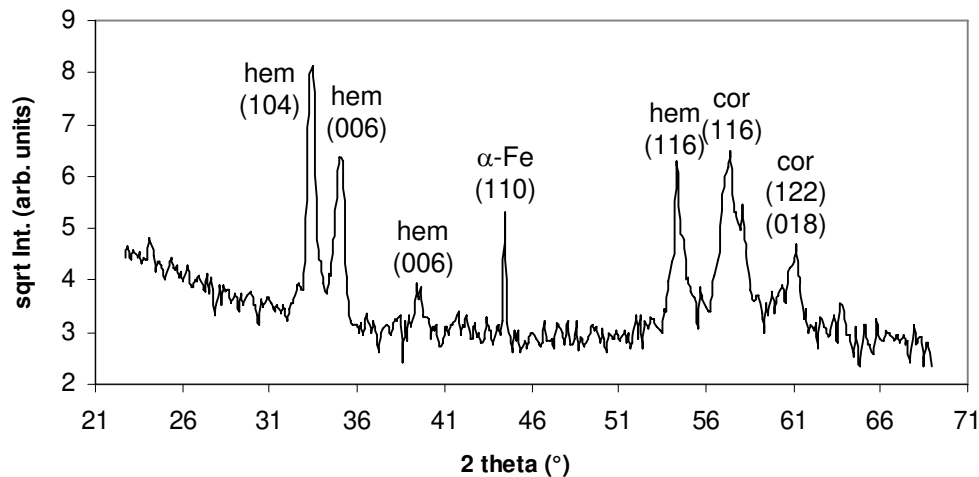


Fig.3: Fe-15at.%Al oxidised at 900°C / 5min / syn.air; incidence angle (θ) = 0.3° (interaction depth ~ 600 nm); phases identified: hematite, corundum and α -Fe structure.

b) in N₂-5vol.%H₂ (dew point -40°C)

The oxidation of Fe-15at.%Al samples at 700°C, 800°C and 900°C for 5 minutes in N₂-5vol.%H₂ (dew point -40°C) gas mixture leads, according to SEM results, to the formation of iron crystals on the surface and an Al oxide layer underneath. The XPS measurements show the thickness of the oxide layer ranging from 0.5 μ m (700°C) to more than 1.5 μ m for higher temperatures. The present XRD measurements confirmed the presence of α -Fe at all temperatures. Very weak corundum reflections were observed only for the sample oxidized at 900 °C (Figure 4).

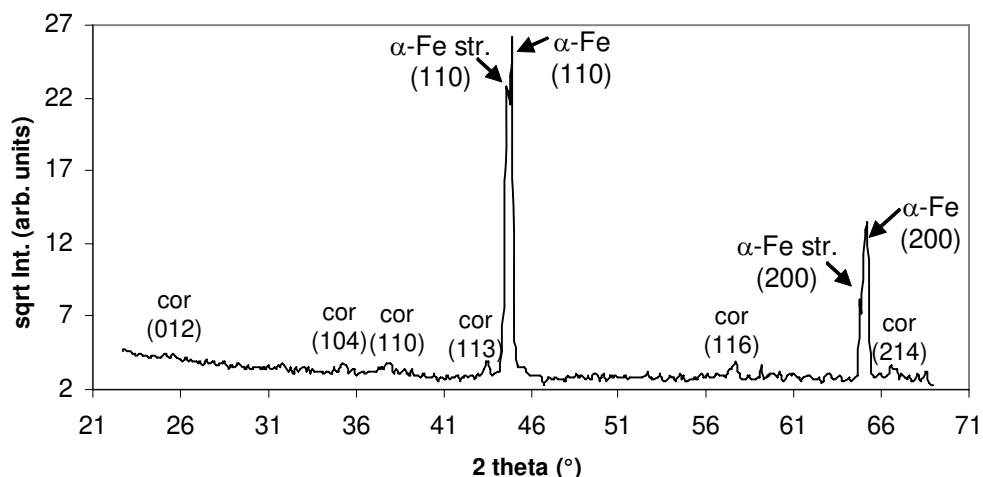


Fig.4: Fe-15at.%Al oxidised at 900°C / 5min / in N₂-5vol.%H₂ (d. p. -40°C) g. m.; incidence angle (θ) = 0.3° (interaction depth ~ 600 nm); phases identified: α -Fe structure (matrix), α -Fe and corundum.

**2. Fe-26at.%Al-4at.%X (with X = 0, Ta Ti and Nb) oxidised at 700°C:
a) in synthetic air.**

The results obtained at Fe-26 at.% Al at 700°C in air are similar to those of Fe-15 at.% Al. The XRD analysis reveals both hematite and corundum phases. Oxidation of ternary alloys gets complicated by formation of third element oxides and laves phases. The measured Fe-26at.%Al-4at.%Nb (others were skipped due to time limitation) yield both hematite and corundum as well as Fe₂Nb laves phase (Fig.5).

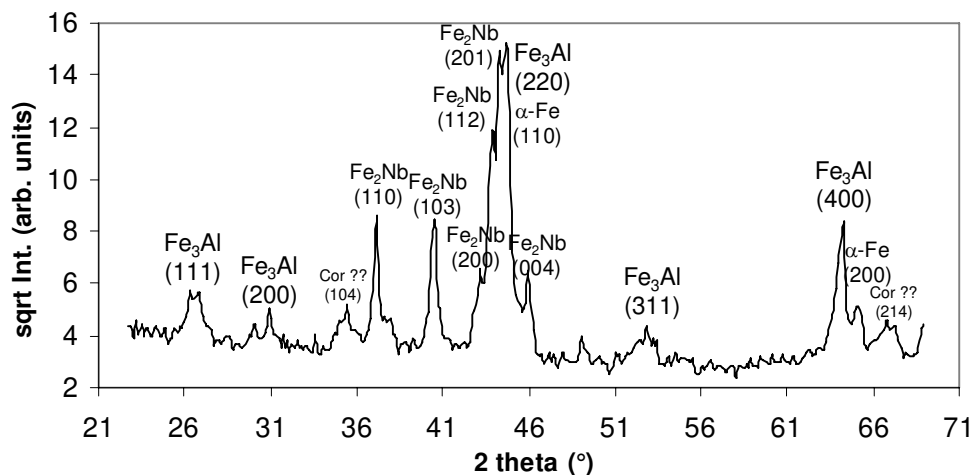


Fig.5: Fe-26at.%Al-4at.%Nb oxidised at 700°C / 5h / in synthetic air, incidence angle (θ) = 0.3° (interaction depth ~ 600 nm); phases identified: Fe₃Al (matrix), α -Fe, Fe₂Nb, the corundum phase is not well identifiable.

b) in N₂-5vol.%H₂ (dew point -40°C) gas mixture.

Similar to the Fe-15at.%Al the oxidation of Fe-26at.%Al-4at.%X (with X = 0, Ta Ti and Nb) at 700°C in N₂-5vol.%H₂ (dew point -40°C) gas mixture leads to the formation of pure iron crystals on the surface and Al oxide layer underneath. SEM and TEM results shows that oxidation of ternary alloys such as Fe-26at.%Al-4at.%Ta and Fe-26at.%Al-4at.%Nb forms an additional superstructure on the surface consisted of laves phase and corresponding Ta or Nb oxide. Oxidation of Fe-26at.%Al-4at.%Ti is more complicated by the formation of Ti oxide rarely located on the surface. As an example figures 5 and 6 show the grazing incidence diffractograms of Fe-26at.%Al-4at.%Nb and Fe-26at.%Al-4at.%Ti.

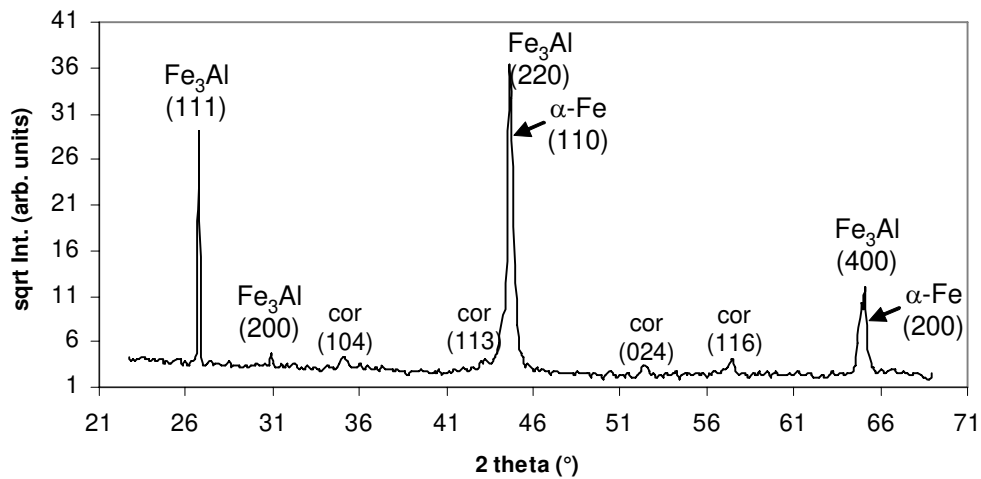


Fig.6: Fe-26at.%Al-4at.%Ti oxidised at 700°C / 5h / in N₂-5vol.%H₂ (d. p. -40°C) g. m.; incidence angle (θ) = 0.3° (interaction depth ~ 600 nm); phases identified: Fe₃Al (matrix), corundum and α -Fe.

Investigation of the Orientation Relationship Between α -Chitin and Calcite in Crab *Cancer pagurus* Cuticle Using Synchrotron x-ray Diffraction at BL-9 Beamline of DELTA Synchrotron Facility.

Ali Al-Sawalmih^{1,*}, Sangbong Yi², Helge Fabritius¹, Dierk Raabe¹

¹Max-Planck-Institut f. Eisenforschung, Max-Planck-Str. 1, 40237 Düsseldorf.

²Technische Universität Clausthal, Agricolastr. 6, 38678 Clausthal-Zellerfeld.

*correspondance address: a.al-sawalmih@mpie.de.

Abstract:

Crab *Cancer pagurus* cuticle contains α -chitin organic fibers associated with crystallites of calcite, embedded in a protein matrix. In this study, x-ray pole figure analysis was performed to investigate the crystallographic texture (preferred orientation) of crystalline calcite and α -chitin, with respect to their orientation relationship in crab *Cancer pagurus* cuticle using synchrotron wide-angle x-ray diffraction (XRD), at the beamline BL-9 –DELTA synchrotron facility. The importance of crystallographic texture in biological materials lies in its direct relationship with its possible role of the contained macromolecules in controlling the epitaxy of the minerals during the biomineralization process. This study shows that crab cuticle reveal a strong crystallographic texture and preferred orientation correlation between the orientation distribution of calcite and α -chitin. It was observed that the *c*-axis of the hexagonal calcite and the *b*-axis of the orthorhombic α -chitin are firstly preferentially aligned parallel to each other and secondly oriented along the surface normal, whereas the other axes are co-aligned with respect to each other throughout the cuticle surface. The spatial rotational freedom of the *c*-axis (fiber axis) of α -chitin is in accordance with the plywood structure of the α -chitin fibers as observed in scanning electron microscopy (SEM). The synchrotron x-ray crystallographic texture results gave for the first time a statistical description of the orientation relationship between the organic and inorganic components in arthropod cuticle, consistent with the same orientation relationship for lobster cuticle carried out at ANKA synchrotron facility. This result strongly suggests that the fibrous structure of α -chitin assists the growth of calcite crystals in crustacean cuticle by functioning directly or indirectly as a template for nucleation and subsequent growth of calcite on the basis of oriented nucleation and epitaxial growth of calcite.

Methods:

Preferred orientation of crystals (or crystallographic texture) in polycrystalline material is conventionally measured by x-ray diffraction after considering some specific Bragg reflections of the content materials. Our experiments were performed employing x-rays of a wavelength of $\lambda = 0.8 \text{ \AA}$ in the transmission mode at the BL-9 beamline of the DELTA synchrotron facility.

At BL-9 beamline (DELTA), crab sample (1x1x10mm) was mounted vertically on the goniometer head in a six-circle goniometer equipped with a MAR-345 detector mounted perpendicular to the primary beam. One data set for each sample consisted of a series of frames recorded with a MAR-345 detector for a sequence of rotations around (φ -axis (sample L-axis)), as defined in Fig. 1, from 0° to 180° in 60 steps each providing one single Debye-Scherrer diagram. Exposure times ranged from 60 to 180 seconds.

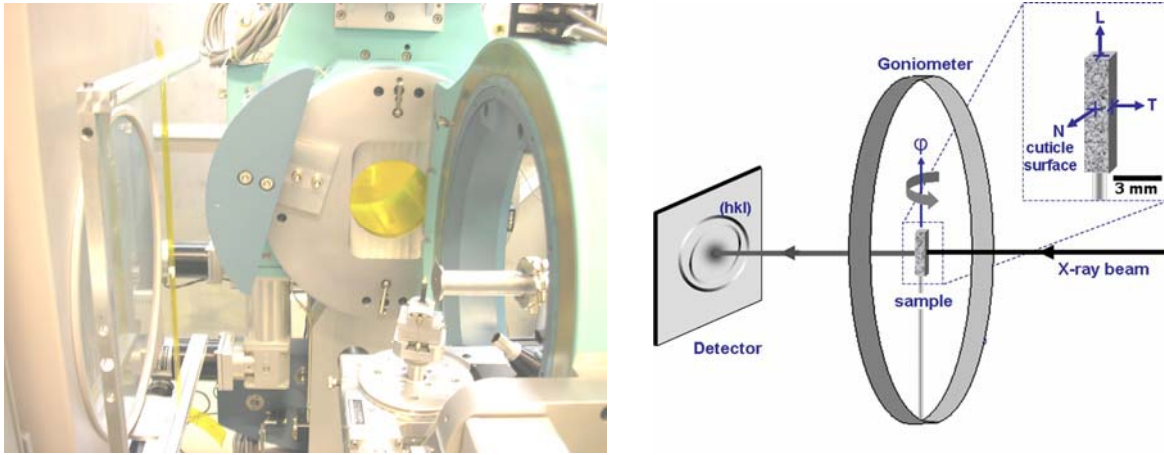


Fig. 1: Image of the diffraction setup of the BL-9 beamline at DELTA synchrotron facility (left), and schematic of the x-ray setup used for pole figure measurements and the local sample coordinates (right).

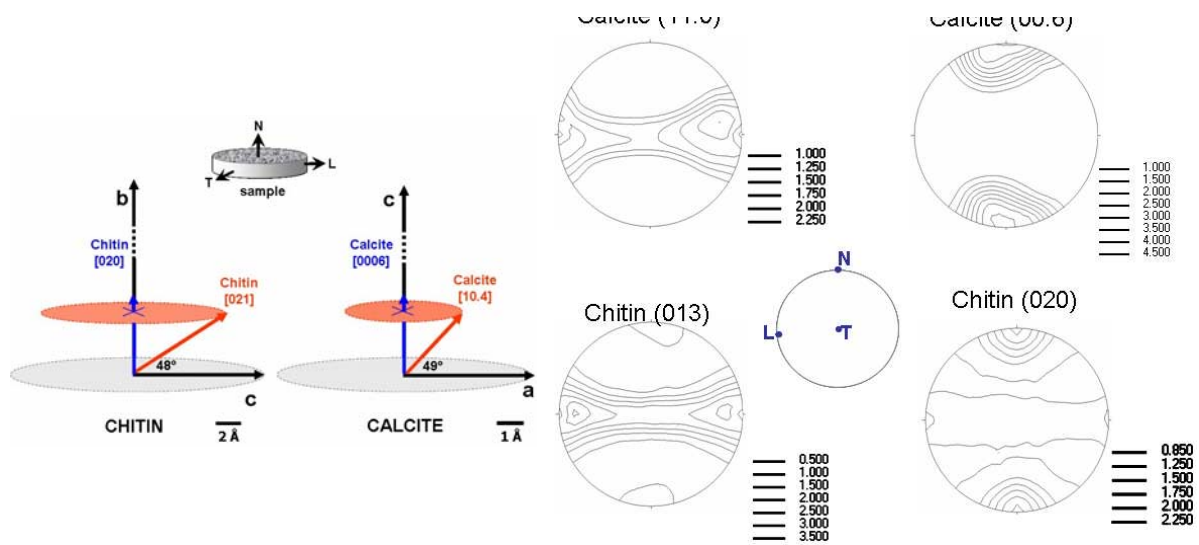


Fig. 2: Schematic shows the orientation of α -chitin and calcite in crab cuticle, with respect to the sample geometry (left) and pole figures of reflection from α -chitin and calcite used to identify the orientation relation between the two phases with respect to the cuticle geometry. The sample reference system is included.

Results:

The complete sets of the pole figures of α -chitin ($\{020\}$ and $\{013\}$) and calcite ($\{00.6\}$ and $\{11.3\}$) are shown in Fig. 2. The $\{020\}$ pole figure of α -chitin indicates the orientation distribution of the longest crystallographic axis of the lattice cell $b=18.86 \text{ \AA}$, while the $\{00.6\}$ pole figure of calcite represents the orientation of the c -axis. The local reference system used for each pole figure is included.

In Fig. 2, a geometrical interpretation of these crystallographic texture results were presented; α -chitin has a strong $\{020\}$ crystallographic texture parallel to N -direction so that the result shown in the pole figures translates into the orientation relationship: the c -axis (calcite) $\parallel b$ -axis (chitin) \parallel exoskeleton surface direction N . We find not only an excellent match of the orientation but also of the absolute numbers of the axis lengths of the two abutting crystal structures; the c -axis of the calcite lattice has a length of 17.062 \AA which is close to the length of the corresponding b -axis of the α -chitin lattice which has an extension of 18.86 \AA . These two lattice directions point both toward the local normal directions of the specimens N .

Conclusions:

- i. X-ray diffraction measurements were carried out using synchrotron x-ray diffraction to study the crystallographic orientation relationship of α -chitin and calcite in the crab cuticle using crystallographic texture analysis established in materials science.
- ii. Crab cuticle reveals a strong crystallographic texture and a correlation relationship between the orientation of calcite and α -chitin was observed; the c -axis of the hexagonal calcite and the b -axis of the orthorhombic α -chitin were preferentially aligned parallel to each other and oriented along the surface normal.
- iii. α -chitin fiber axis (the c -axis) is randomly co-aligned and freely rotated throughout the cuticle surface plane, which is in accordance to the observed plywood structure of chitin fibers using SEM.
- iv. Crystallographic texture in biological materials can explain the control of the contained macromolecules on the orientation of the associated biominerals through biomineralization process.
- v. Indicating a close relationship of unit cell dimension between the c -axis of calcite and the b -axis of α -chitin as well as their identical orientation correlation strongly suggest that the fibrous structure of α -chitin assists the orientation of calcite crystals in crustacean cuticle by functioning directly or indirectly as a template for nucleation and epitaxial growth of calcite.

Acknowledgement:

I thank Dr. Christian Sternemann and Christof Krywka for their assistance and support during our beamtime.

References:

- [1] D. Raabe, A. Al-Sawalmih, P. Romano, C. Sachs, H-G. Brokmeier, S-B. Yi, G. Servos, and HG. Hartwig, *Structure and crystallographic texture of arthropod bio-composites*, Materials Science Forum **495 - 497** (2005), 1665-1674.
- [2] D. Raabe, P. Romano, C. Sachs, A. Al-Sawalmih, HG. Brokmeier, SB. Yi, G. Servos, and H.G. Hartwig, *Discovery of a honeycomb structure in the twisted plywood patterns of fibrous biological nanocomposite tissue*, J. Cryst. Growth **283** (2005), 1.
- [3] D. Raabe, P. Romano, C. Sachs, H. Fabritius, A. Al-Sawalmih, SB.. Yi, G. Servos, and H.G. Hartwig, *Micro structure and crystallographic texture of the chitinprotein network in the biological composite material of the exoskeleton of the lobster homarus americanus*, Mat. Sci. Eng. A **421** (2006), 143.
- [4] D. Raabe, C. Sachs, and P. Romano, *The crustacean exoskeleton as an example of a structurally and mechanically graded biological nanocomposite material*, Acta Materialia **53** (2005), 4281.
- [5] C. Krywka, M. Paulus, C. Sternemann, M. Volmer, A. Remhof, G. Nowak, A. Nefedov, B. Poter, M. Spiegel, and M. Tolan, *The new diffractometer for surface x-ray diffraction at beamline bl9 of delta*, J. Synchrotron Radiation **13** (2006), 8-13.

X-ray standing waves created by synchrotron radiation and computer programs

Markus Krämer, Alex von Bohlen, Roland Hergenröder, ISAS Dortmund
Christian Sternemann, Michael Paulus, DELTA, Universität Dortmund

With the technique of X-ray standing waves (XSW) it is possible to characterize thin films, layered structures and surface depositions as well as element concentration distributions on a nanometer scale. XSW measurements are fast, easy and element specific and several elements can be observed simultaneously by an energy dispersive detector. The obtained measurements represent the element distribution and a characterization in depth of the layer-structure of the observed samples. Usually little sample preparation is necessary for XSW measurements. Vacuum is not necessary in most cases and XSW can be performed on conducting and non-conducting samples making it a very versatile technique.

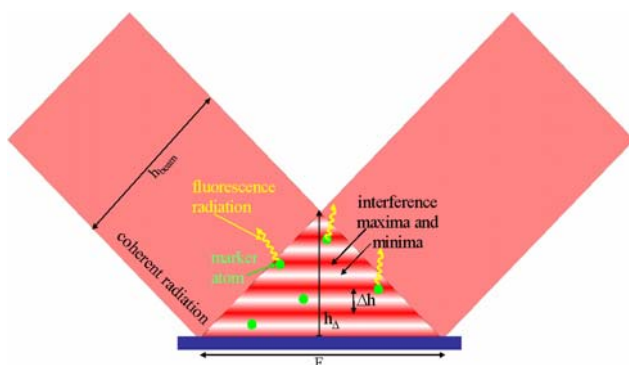


Fig. 1: Schematic illustration of the generation of X-ray standing waves. An incident beam is reflected at a surface. In a triangular region reflected and incident waves interfere and form a periodic intensity structure.

Synchrotron radiation as photon source for XSW measurements has several advantages: The photon flux is much higher than the flux from an X-ray tube, photon energy can be chosen in a wide range from below 1 keV to more than 30 keV to utilize the energy most suitable for a certain kind of sample, and radiation is sufficiently monochromatic and longitudinally coherent enough to generate desired X-ray Standing Waves. Thus various kinds of thin film and multilayer samples have been observed at DELTA using XSW.

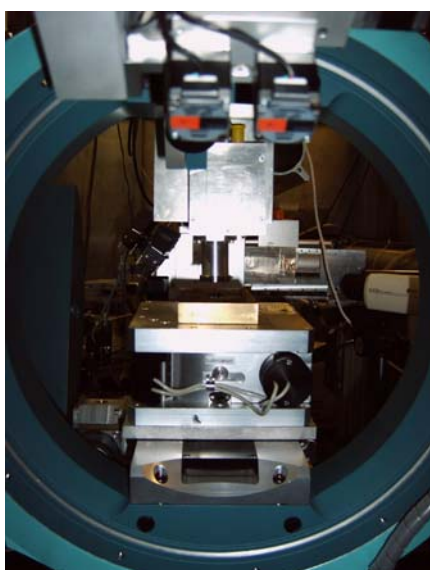


Fig. 2: Experimental set-up for XSW measurements at DELTA. The beam is incident from the side and reflected at the sample. Fluorescence is detected by an energy dispersive detector above the sample at variable angles of incidence.

Interpretation of XSW scans requires extensive calculation with increasing complexity for complicated sample structures. Further, idealized layered structure models have to be replaced

by more realistic models with rough interfaces, exponential decay of element concentrations and others. To handle this task a versatile computer program was developed that allows calculation of XSW intensity distributions in a wide variety of sample systems and comparison of these calculations to measured data.

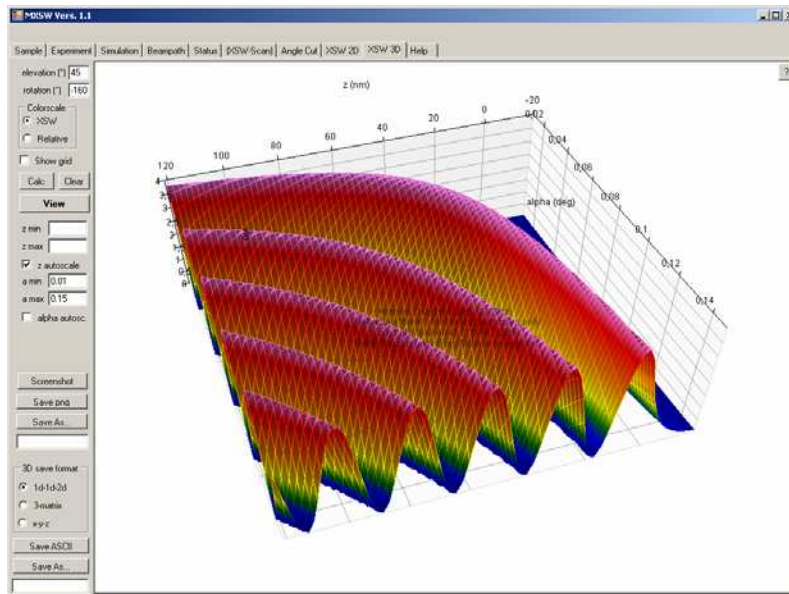


Fig. 3: Calculated "3D" XSW intensity distribution above a flat silicon substrate. 3D means intensity versus angle of incidence and position above the reflecting surface.

Further, the development of an automated fitting option using evolutionary algorithms for this program is in progress. Both the simulation program as well as results obtained from measurements performed at SAW beamline (BL9) will be presented in a talk.

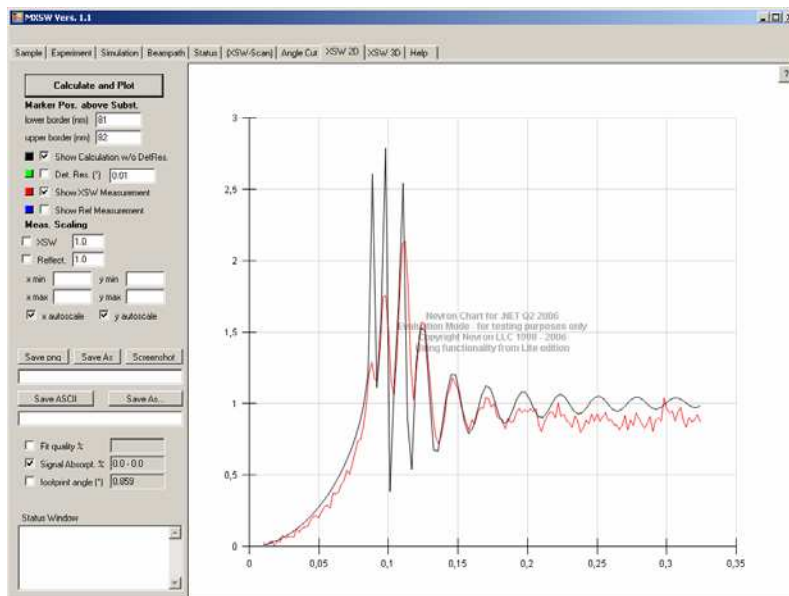


Fig. 4: Measured XSW intensity and calculated fit from the computer program showing intensity versus angle of incidence.

Literature

1. M. Krämer, A. von Bohlen, C. Sternemann, M. Paulus, R. Hergenröder. X-ray standing waves: A method for ultrathin layered systems. *J. Anal. Atom. Spec.*, 21 (2006) 1136-1142.
2. M. Krämer, A. von Bohlen, C. Sternemann, M. Paulus, R. Hergenröder. Synchrotron Radiation Induced X-ray Standing Waves Analysis of Layered Structures. *Appl Surface Sci* (2006) in press.

First Results of the Characterization of the VUV-Beamline U55 (BL11) at DELTA

Sven Döring, Ulf Berges and Carsten Westphal

*DELTA, University of Dortmund, Maria-Goeppert-Mayer-Str. 2, Dortmund, Germany
Experimental Physics I, University of Dortmund, Otto-Hahn-Str. 4, Dortmund, Germany*

During 2006 commissioning of BL 11 continued parallel to further in house experiments. Today the procedures that are necessary to characterize the beamline are understood and can be conducted to achieve data comparable to BESSY II. Up to now the first of two gratings is characterized. The energy-calibration with this 400 lines/mm grating is done and the energy-resolution is measured for the low- and medium-resolution range.

Using a ionisation-chamber the exact energy of the synchrotron radiation can be measured. Figure 1 shows the Nitrogen 1s-3p transition-spectrum measured at BL 11. The spectrum consists of a couple of lines, so called vibrational levels. The natural line-width is Lorentz-shaped. The measured spectrum shows the convolution of these lines with the Gaussian width of the monochromator's resolution. Thus to the data a sum of five Voigt-functions is fitted. For each peak the amplitude and the position is a free fit-parameter while the line-width is the same for all peaks. The Lorentzian line-width is kept fixed at 115 meV according to [1]. The energy-resolution is given by the Gaussian width which is a fit-parameter. Figure 1 shows a spectrum with a Gaussian line-width of $108 \text{ meV} \pm 5 \text{ meV}$ according to a energy-resolution of $E/\Delta E \sim 3700$.

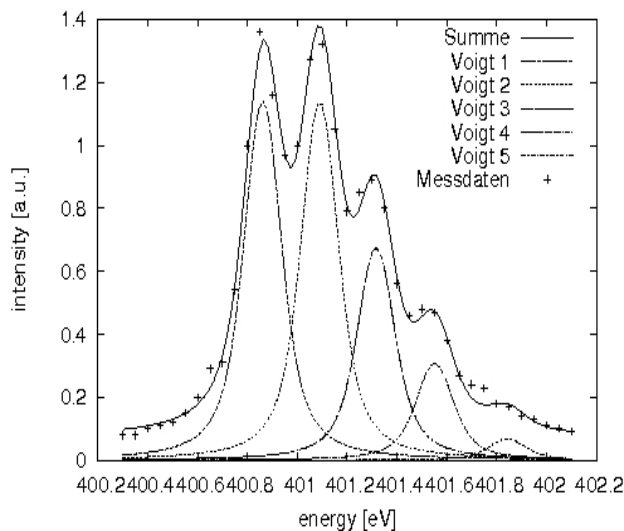


Figure 1: A sum of five Voigt-functions fits to the measured Nitrogen-spectrum. The Gaussian linewidth representing the resolution is 108 meV

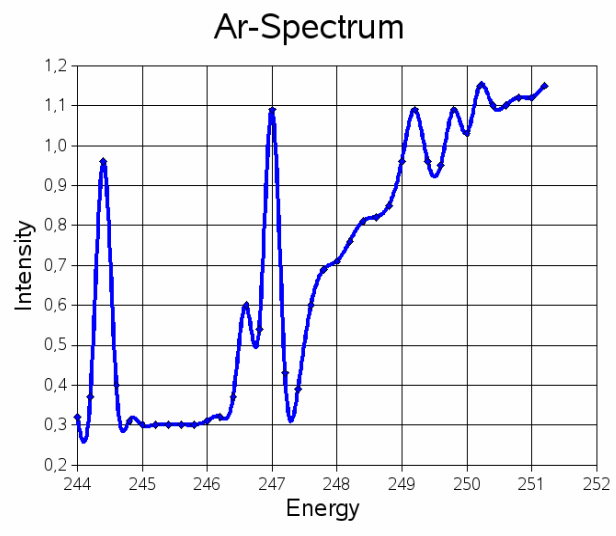


Figure 2: The Argon-spectrum shows its first peak at 244.4 eV and proves the correctness of the energy-calibration.

By measuring the same spectrum at different c_{FF} -values the energy-calibration can be conducted according to [2]. Afterwards the calibration can be checked by measuring different transition-spectra of different gases according to [1]. Figure 2 shows a part of the Argon-spectrum in the range of the 2p-4s resonance. According to [1] this peak is at exact the right position of 244.4 eV . This example shows that the energy-calibration is correct.

Further measurements with other gases such as Oxygen and Neon show the same result. All peaks could be found at the right positions with errors smaller than 0.1 eV.

A photo-diode behind mirror 4 just in front of the experiment at the end of the beamline is used to measure the photon-flux of the beamline. With the help of calibration-curves from the electrical current the photon-flux can be calculated and scaled for an electron-beam-current of 100 mA in the storage-ring. Figure 3 shows the flux in the energy-range from 150 to 800 eV.

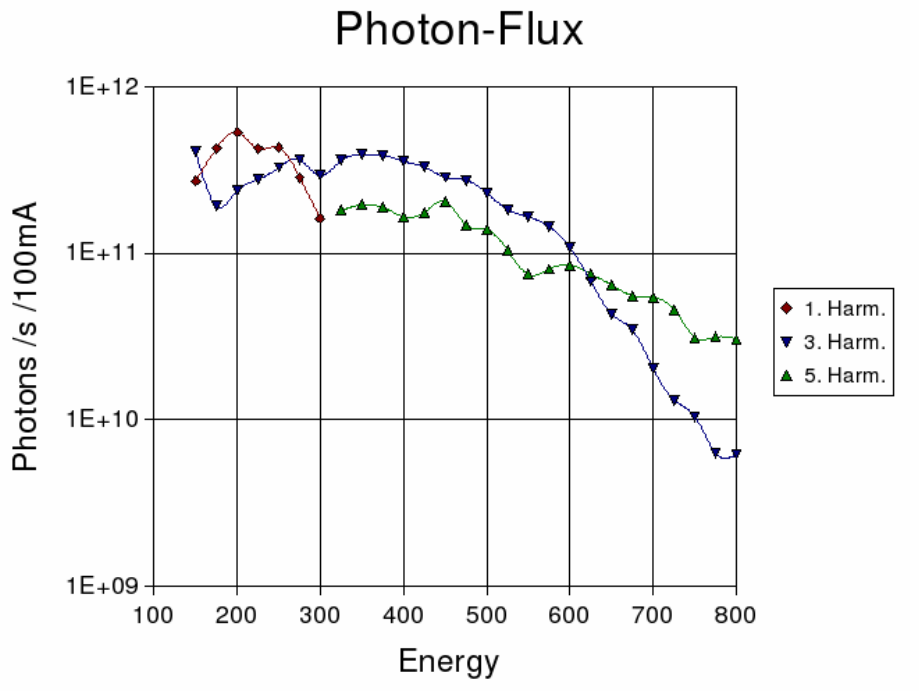


Figure 3: The Photon-Flux at BL 11 measured with a photo-diode at the end of the beamline just in front of the experiment. The figure shows which undulator-harmonic is to be used depending on the energy to gain the maximal flux.

The authors would like to thank Rolf Follath from BESSY for his help at highly appreciated discussions of our measurements and procedures. We also thank the DELTA staff for their support.

[1] Fedoseenko, S. I. ; Vyalikh, D. V. ; Iossifov, I. E. ; Follath, R. ; Gorovikov, S. A. ; Püttner, R. ; Schmidt, J.-S. ; Molodtsov, S. L. ; Adamchuk, V. K. ; Gudat, W. ; Kaindl, G.: Commissioning results and performance of the high-resolution Russian-German Beamline at BESSY II. In: Nuclear Instruments and Methods in Physics Research A 505 (2003), S. 718-728

[2] Weiss, M. R. ; Follath, R. ; Sawhney, K. J. S. ; Zeschke, T.: Absolute energy calibration for plane grating monochromators. In: Nuclear Instruments and Methods in Physics Research A 467 (2001), S. 482-484

Ultrathin films of HfO₂ on Si(100) upon annealing

C. Flüchter^{1,2,*}, A. de Siervo³, D. Weier^{1,2}, M. Schürmann¹, U. Berges^{1,2}, M.F. Carazzolle⁴, R. Landers^{3,4}, G.G. Kleiman⁴, C. Westphal^{1,2},

¹ Experimentelle Physik 1 - Universität Dortmund, Otto-Hahn-Str.4, D 44221 Dortmund, Germany

² DELTA - Universität Dortmund, Maria-Goeppert-Mayer-Str. 2, D 44227 Dortmund, Germany

³ Laboratório Nacional de Luz Sincrotron, C.P. 6192, 13084-971 Campinas, SP, Brazil

⁴ Instituto de Física - Universidade Estadual de Campinas, C.P. 6165, 13083-970 Campinas, SP, Brazil

* corresponding author: christian.fluechter@uni-dortmund.de

(November 2006)

In order to increase the switching speed and the efficiency of modern semiconductor devices a further down scaling is desired. Thus, the SiO₂ gate dielectric in MOSFETs (Metal Oxide Semiconductor Field Effect Transistors) has to be replaced by layers of a material with a much higher dielectric constant like HfO₂ or ZrO₂ [1,2]. A major concern of these systems is their thermal stability. Annealing processes usually lead to silicidation of the hafnium (or zirconium) at the interface.

In this work, ultrathin films of HfO₂ on Si(100) were prepared and investigated by means of photoelectron spectroscopy (XPS), low-energy electron diffraction (LEED) and X-ray photoelectron diffraction (XPD) in order to clarify the structure of the HfO₂/Si(100) interface. Synchrotron light with an energy of $h\nu=200$ eV was used for excitation.

The measurements were conducted at the the undulator beamline 11 at DELTA. The primary energy can precisely be selected by a plane grating monochromator (PGM) and was set to an energy of 200 eV for our experiments. The spot of the beam at the sample site has a size of around $70 \times 100 \mu\text{m}$. Ultrathin layers of hafnium oxide ($< 10 \text{ \AA}$) were deposited onto the Si(100) samples by a specially prepared electron beam evaporator. After the evaporation the samples were heated in consecutive cycles from 200°C up to 750°C. To follow the evolvment of the system, high-resolution XPS spectra and LEED pictures were recorded after each cycle. In addition, XPD patterns were recorded after the first and the last cycle.

Figure 1(a) displays a photoemission spectrum of the Si 2p state directly after the evaporation. One of the challenges in the preparation of this system is to prevent the formation of SiO₂. The chemical shift between the 2p photoelectron signal of bulk silicon and the corresponding signal of SiO₂ is around 4 eV and can be identified in a high-resolution XPS spectrum. At the position of the Si⁴⁺ component, marked by the arrow in Fig. 1(a), no electron yield is obtained. However, several sub-oxides can be identified close to the silicon bulk signal. Those can be ascribed to interface components between the Si and the HfO₂.

Figure 1(b) displays the corresponding Hf 4f photoelectron spectrum directly after the evaporation. The formation of HfSi₂ would be indicated by electron contributions at the position marked by the arrow. The spectrum shows that also the formation of HfSi₂ could be avoided.

During the cumulative annealing of the system the formation of SiO₂ could be observed again. At temperatures above 700°C the oxide transformed into HfSi₂. The next step will be to record photoelectron diffraction patterns from the interface components of the system at different stages of annealing.

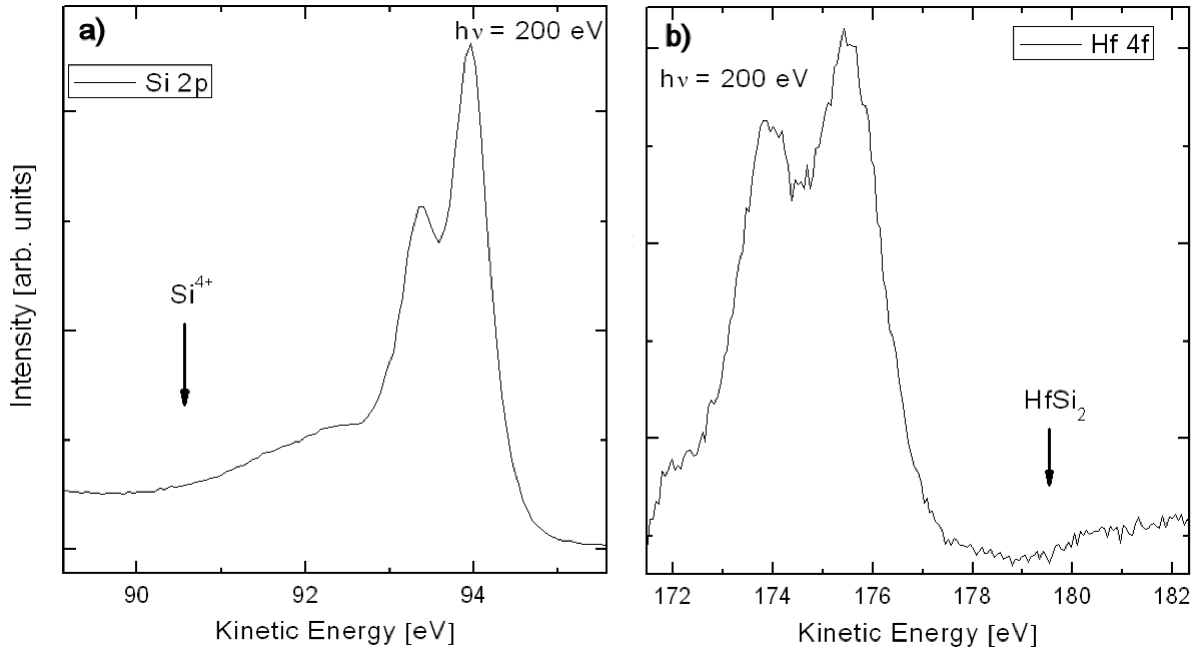


Figure 1: Si 2p photoelectron signal (a) after the evaporation of HfO_2 . Several sub-oxide components are visible, but no SiO_2 . Hafnium 4f signal (b) directly after the evaporation. The chemical shift indicates that hafnium is only bond to oxygen and not to silicon or other hafnium atoms.

We investigated the system $\text{HfO}_2/\text{Si}(100)$ by means of photoelectron spectroscopy and photoelectron diffraction. It was possible to deposit HfO_2 on the surface by electron beam evaporation without the initial formation of SiO_2 or HfSi_2 . Cumulative heating of the system led to the formation of Si^{4+} components in the silicon photoelectron signal. By annealing at temperatures above 700°C the HfO_2 was transformed into HfSi_2 , forming island on the silicon surface. The temperature dependence of the interface components of the system was followed by high-resolution XPS-spectra.

For further investigations it is planned to passivate the silicon surface by nitrogen exposure to form a Si_3N_4 diffusion barrier. In comparable investigations [3] it could be shown that the oxygen diffusion into the silicon bulk can be noticeably reduced by the presence of nitrogen at the interface.

- [1] G.D. Wilk, R.M. Wallace, J.M. Anthony, J. Appl. Phys., **89**, 5243 (2001)
- [2] C. J. Först, C.R. Ashman, K. Schwarz, Nature, **427**, 53 (2004)
- [3] M. R. Visokay, J. J. Chambers, A. L. P. Rotondaro, A. Shanware, L. Colombo, Appl. Phys. Lett. **80**, 3183 (2002)

Investigation of the radiation damage on SAM of aromatic thiolates

D. Weier^{1,2,*}, C. Flüchter^{1,2}, M. Schürmann¹, U. Berges^{1,2}, S. Döring^{1,2}, C. Westphal^{1,2}

¹ Institute of Physics - University Dortmund, Otto-Hahn-Str.4, D 44221 Dortmund, Germany

² DELTA - University Dortmund, Maria-Goeppert-Mayer-Str. 2, D 44227 Dortmund, Germany

* corresponding author: daniel.weier@uni-dortmund.de

SAM (Self-assembled-monolayers) of aromatic thiolates have been studied in the last three decades for many kinds of interests. The amphiphilic molecules with a chainlike structure consist of a hydrophobic head group and a hydrophilic carbon chain part. This structure of the molecules allows to chemisorb the molecules in close packed arrays onto well prepared surfaces with a high affinity to the sulfur head group. The most frequently investigated surfaces for these systems are Au and Ag. SAM surfaces provide a way to manipulate surface properties such as wetting, adhesion, lubrication and corrosion[1]. Another very interesting field for the application of SAMs is in application in electronic devices. The pi electron configuration of the molecules allows to tune the resistivity of the molecules which is very interesting for possible applications in integrated circuits.

An important trait of the molecules is their strong interaction with X-ray radiation and electrons. This interaction is for example used for lithographic purposes[2]. However, this interaction is one of the main problems while studying these films with standard techniques like LEED and photoelectron spectroscopy. On one hand it is necessary to have a high brilliance photon source to achieve an adequate counting statistics with good resolution for the sulfur 2p line, on the other hand a high photon flux leads to a noticeable radiation damage in the films. The problem of radiation damage inside the focus of an undulator beamline is well known[3]. In this project a way had to be found to deal with this problem by moving the sample out of the focus of the beamline.

In this work we investigated C12 ($\text{CH}_3\text{-(CH}_2\text{)}_{11}\text{-SH}$) molecules on Au surfaces. The investigated SAMs were chemisorbed onto an approximately 300 nm thick gold film by immersing them for 24h to a 1 mMol solution of the respective substance. The 300 nm gold films were evaporated onto mica. This evaporation leads to polycrystalline films. All measurements were performed in an ultrahigh vacuum chamber with a base pressure of $5 \cdot 10^{-11}$ mbar at the beamline 11 in DELTA.

The first measurements were performed inside the focus of the beamline to have comparable results for the same synchrotron source and the same beamline inside and outside of the focus.

For the undamaged film the sulfur atoms are bonded to one gold atom and one carbon atom. In this configuration the binding energy of the sulfur 2p is 162.0 eV and 163.3 eV. In figure 1 binding energies are given with respect to the S 2p_{3/2} component. In the molecules with radiation damage the sulfur atoms are doublebonded to carbon instead of gold and carbon. This leads to a chemical shift of 1.3 eV with respect to the sulfur 2p peak for the undamaged films.

Figure 1(a) shows an out-of-focus measurement without radiation damage but this spectra. Figure 1(b) shows in-focus measurements of the sulfur 2p photoemission spectrum. The different measurements belong to different stages of radiation damage in the films. As can clearly be seen, the molecules are subject to a distinct radiation damage after a short time of measurement.

This leads to the conclusion that it is impossible to achieve reasonable results for long time measurements (e.g. photoelectron diffraction) inside the focus of the beamline.

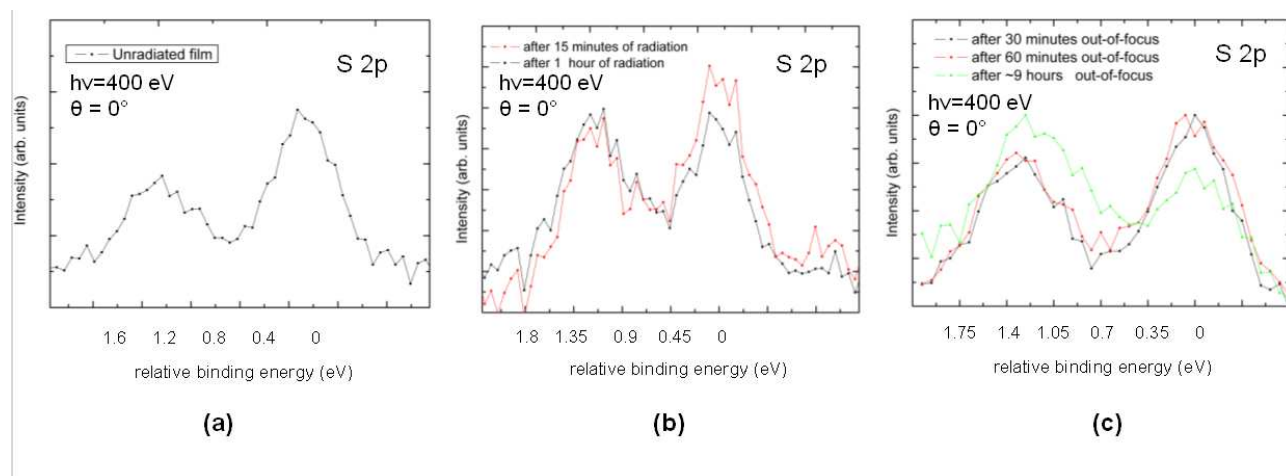


Figure 1: Sulfur 2p spectra for different stages of radiation. (a) unradiated, (b) inside the focus, (c) out of focus ($h\nu = 400$ eV)

For the out-of-focus measurements the sample was mounted 0.5 meters away from the focus position. Ray tracing calculations proposed that this should lead to an enlargement of the beam size by a factor of approximately 100. The original beam size inside the focus of the beamline is approximately $100 \mu\text{m}^2$, therefore the new beam size should be around 1mm^2 . With a illuminated sample area of 1mm^2 it is still possible to collect all the electrons with the photoelectron spectrometer without losing angular resolution. This means, that the same energy resolution and the same flux can be achieved, while there will be a smaller radiation damage at the sample due to the smaller number of photons per sample area outside of the focus.

Figure 1(c) shows the out-of-focus measurements taken at beamline 11. As can clearly be seen, the radiation damage is smaller less for the same exposure time to synchrotron light. In reverse this means that it is possible to perform long-time measurements with the same sample out of the focus.

In conclusion it was shown that it is possible to decrease the temporal radiation damage by moving the sample out of the focus of the beamline. The time window leading to strong radiation damage at the sample could be increased from several minutes to some hours.

This will allow us to perform long time measurements at aromatic thiolates in the future. For example photoelectron diffraction investigations become possible. With photoelectron diffraction it will be possible to get information about the hidden interface between the gold substrate and the aromatic thiolates.

Acknowledgments

The authors would like to thank M. Zharnikov for providing the samples. We also thank the staff of DELTA for the support during beamtimes.

- [1] A. Ulman, Chem. Rev. **96**, 1533 (1996)
- [2] P.E. Lailinis, Science **254**, 981 (1991)
- [3] K. Heister, M. Zharnikov, M. Grunze, Langmuir **17**, 8 (2001)

STATUS OF THE VUV-BEAMLINES U55 (BL11) AND TGM3 (BL12) AT DELTA

Ulf Berges, Sven Döring and Carsten Westphal

*DELTA, University of Dortmund, Maria-Goeppert-Mayer Str. 2, Dortmund, Germany
Experimental Physics I, University of Dortmund, Otto-Hahn-Str. 4, Dortmund, Germany*

The beamlines U55 (BL 11) and TGM3 (BL 12) in the VUV-range at the storage ring facility DELTA are set up and operated by the group Experimental Physics Ib at the department of Physics of the university of Dortmund. Experiments are performed at the U55-Beamline by this group. The TGM3-Beamline is still under commissioning.

U55-BEAMLINE

The U55-Beamline is working in the energy range between 55 and 1500 eV. The linearly polarized synchrotron radiation is generated by a permanent magnet undulator with a variable gap between 20 and 200 mm as insertion device. The beamline uses a PGM-setup with two gratings (400 and 1200 lines/mm) and a variable exit slit up to 3 mm. The designed photon flux is 10^{10} to 10^{11} photons/s/0.1A @ 20 μm exit slit and 10^{12} to 10^{13} photons/s/0.1A @ 200 μm . The designed energy resolution is up to 30000 @ 20 μm and between 1000 and 8000 @ 100 μm . The expected focus size at the experiment is 70 x 30 μm^2 . The planned experiments are photoemission spectroscopy (XPS) and photoelectron diffraction pattern (XPD) of the interface layer of semiconductors.

The measured photon flux at this diode is about 10^{12} photons/s/100mA @ 200 μm exit slit size. The flux has still to be increased to achieve design values due to the still not completely optimized settings of the beamline elements. The energy resolution has been tested at 400 eV with nitrogen to be about 3700 (see report Döring).

During the synchrotron radiation weeks of DELTA various XPS and XPD experiments at different probes with the experimental chamber of the group have been performed at different beamline energies between 200 and 800 eV (see reports Flüchter and Weier). In between the beamline setup has been improved to achieve a higher photon flux and energy resolution. The actual beamline setup is sufficient for the performed measurements, but still has to be improved for the planned experiments during the next year (photon flux at small exit slit sizes and energy resolution).

Due to an accident the monochromator is not working at the moment and all experiments have been stopped.

TGM3-BEAMLINE

The TGM3-Beamline is a dipole beamline in the energy range between 6 and 200 eV. Planned experiments are photoelectron spectroscopy in the valence band regime and Fermisurface-Mapping. The former BESSYI-beamline has been adapted to the situation at DELTA. The expected photonflux is in the order of the old BESSYI-setup. The optical layout was kept, the vacuum system and diagnostics improved. The beamline is completely build up. The beamline consists of the focusing mirror, entrance slit, monochromator, exit slit and refocusing mirror. Synchrotron radiation has reached the monochromator. Stability measurements concerning the first focusing mirror have been performed. A new chamber for the first mirror has just been delivered to improve the beamline setup. A gascell and photodiode to perform first measurements with beam at the experiment have been integrated into the beamline. The expected photonflux at the experiment is in the order of 10^{11} photons/s/100mA between 30 and 80 eV with the 600 lines/mm grating and 10^{10} photons/s/100mA between 80 and 200 eV with the 1800 lines/mm grating. The beam size at the source point at DELTA is $136 \times 65 \mu\text{m}^2$, the divergence $194 \times 9 \mu\text{rad}^2$. The beam size at BESSYI was three times bigger, the divergence in the same order.